

XMM-Newton study of X-ray sources in the field of Willman 1 dwarf spheroidal galaxy [★]

Sara Saeedi^{1†}, Manami Sasaki²,

^{1,2} *Dr. Karl Remeis-Sternwarte, Erlangen Centre for Astroparticle Physics, Friedrich-Alexander-Universität Erlangen-Nürnberg, Sternwartstrasse 7, D-96049, Bamberg, Germany*

Accepted XXX. Received YYY; in original form ZZZ

ABSTRACT

We present the results of the analysis of three *XMM-Newton* observations of the Willman 1 dwarf spheroidal galaxy (Wil 1). X-ray sources are classified on the basis of spectral analysis, hardness ratios, X-ray-to-optical flux ratio, X-ray variability, plus cross-correlation with available catalogues in optical and infrared wavelengths. We catalogued 97 sources in the field of Wil 1. Our classification shows the presence of a β -type symbiotic star in Wil 1. We classified one M dwarf foreground star in the field of Wil 1. Moreover, fifty-four sources are classified as background AGNs and galaxies. Our study shows that the luminosity of the X-ray sources of Wil 1 does not exceed $\sim 10^{34}$ erg s^{−1} in the energy range of 0.2–12.0 keV, which is similar to observed luminosities of sources in nearby dwarf spheroidal galaxies.

Key words: Binaries: symbiotic – X-rays: binaries – galaxies:dwarf galaxies

1 INTRODUCTION

So far, about thirty dwarf galaxies have been discovered around the Milky Way, with the majority of them being dwarf spheroidal galaxies (dSphs) (e.g. [McConnachie 2012](#)). Studies show that almost all nearby dSphs have an old stellar population, mainly late-type stars with low metallicities (e.g. [Weisz et al. 2014](#); [Tolstoy et al. 2009](#)). These properties make them ideal targets to study the early stages of galaxy evolution. In X-rays, the population of nearby dSphs has been poorly studied so far in comparison to other types of nearby galaxies ([Fabbiano 2006](#)). The close distance of dSphs together with the low absorption towards most of them give us a unique opportunity to search for the population of soft and low-luminosity ($L_x < 10^{34}$ erg s^{−1}) X-ray sources, which are not detectable in distant nearby galaxies. Based on the very old stellar population of dSphs, theoretical models suggest that the presence of persistently bright X-ray binaries is rather unlikely in these galaxies (see e.g. [Maccarone et al. 2005](#)). In recent studies no X-ray binary was confirmed in dwarf galaxies (e.g. [Manni et al. 2014](#); [Arnason et al. 2019](#); [Saeedi et al. 2016](#)). However, some studies show the presence of low luminosity X-ray sources in these galaxies ([Saeedi et al. 2016](#); [Ramsay & Wu](#)

[2006](#)). Our deep study using the *XMM-Newton* observations confirmed the presence of four symbiotic stars in the Draco dSph ([Saeedi et al. 2019](#)). This result shows that in comparison to the X-ray binaries, the presence of accreting white dwarfs is more probable in dSphs, due to the similar time scale of the age of the galaxies and that of the formation of white dwarfs from late-type stars, which are the main population of dSph. Among the different types of accreting white dwarfs ([Mukai 2017](#)), the symbiotic stars (i.e. accreting white dwarf or neutron star with a red giant companion) seem to be more likely to be detected in nearby dSphs. In X-rays, different types of symbiotic stars show a wide range of energy (0.1–100 keV) and luminosity ($10^{31} - 10^{38}$ erg s^{−1}) ([Luna et al. 2013](#); [Mukai 2017](#)). Usually, X-ray sources with luminosities of $\gtrsim 10^{32} - 10^{33}$ erg s^{−1} are detectable in dSphs around the Milky Way owing to their small distances. Moreover, the optical brightness of red giants helps us to identify the nature of the companion star.

To confirm the results of Draco dSph and to provide a wider view of the population of accreting white dwarfs in dSphs, it is necessary to classify the X-ray sources of more dSphs with different stellar populations. Following this goal, we studied the X-ray sources in Willman 1 dSph (Wil 1, hereafter) applying the same multi-wavelength classification methods as for Draco dSph.

Wil 1 (RA=10h49m21s, DEC=+51°03.0′0.0″) is an old dSph, discovered in 2005 by [Willman et al. \(2005\)](#). This galaxy has a stellar mass of $\sim 1.0 \times 10^3 M_\odot$ and is one of the the least massive Milky Way satellites ([Martin et al. 2007](#))

[★] Based on observations obtained with *XMM-Newton*, an ESA science mission with instruments and contributions directly funded by ESA Member States and NASA.

[†] E-mail: sara.saeedi@fau.de

located at a distance of 38 ± 7 kpc (McConnachie 2012). Its half-light radius (r_h) is $2.3'$ (~ 20 pc) (Willman et al. 2011). The age of the galaxy is estimated to be ~ 10 – 14 Gyr and its metallicity is $-2.0 \lesssim [\text{Fe}/\text{H}] \lesssim -1.0$ (Martin et al. 2007; Willman et al. 2011). Draco and Wil 1 dSphs have similar ages and metallicities (McConnachie 2012). However, with a stellar mass of $\sim 2.9 \times 10^5 M_\odot$ and r_h of ~ 220 pc for Draco dSph (McConnachie 2012), the stellar density of Wil 1 is $\sim 40\%$ of that of Draco dSph.

Wil 1 has been observed three times with *XMM-Newton* in 2010 with the aim to detect an emission line from decaying dark matter (Loewenstein & Kusenko 2012). These observations had never been used for X-ray source classification in the field of Wil 1. The exposure time of *XMM-Newton* observations of Wil 1 was long enough to perform X-ray spectral and timing analyses for the bright X-ray sources in the field of this galaxy. As Willman et al. (2011) have shown, the main stellar population of Wil 1 is located inside $3r_h$ of this dSph. Only 1% of stars, which belong to Wil 1 are exponentially distributed beyond $4r_h$. In this paper, we report the details of the X-ray analysis together with multi-wavelength studies, which have been performed to classify the X-ray sources in the field of Wil 1. In Sect. 2 we describe the data reduction and analysis of the *XMM-Newton* observations. In Sect. 4 and Sect. 5 we present the multi-wavelength studies and X-ray methods, which are used to classify the X-ray sources. In Sect. 6 we explain the properties and the classification of the detected sources in the field of Wil 1.

2 DATA REDUCTION

Wil 1 has been observed in three *XMM-Newton* observations, which are listed in Table 1. Full-frame mode and the thin filter were used for cameras EPIC-pn (Strüder et al. 2001) and EPIC-MOS1,2 (Turner et al. 2001) in all observations. Data reduction and source detection were performed using the *XMM-Newton* Science Analysis System (SAS, V.17.0.0). High background caused by soft proton flares were screened from the event files. Threshold rate of ≤ 0.35 counts $^{-1}$ for EPIC-MOS and rate ≤ 0.4 counts $^{-1}$ for EPIC-pn are applied to find good time intervals. Light curves of clean event lists were also checked visually to remove possible background flares. Table 1 lists the net exposure time for each observation and EPIC camera. Source detection in the five standard energy-bands of *XMM-Newton* B1 (0.2–0.5 keV), B2 (0.5–1.0 keV), B3 (1.0–2.0 keV), B4 (2.0–4.5 keV), B5 (4.5–12.0 keV) was performed using the SAS task `edetect-chain` for each observation. We selected the minimum value of maximum likelihood (L) of 10 for the source detection. Probability of Poisson random fluctuations of the counts (p), which is based on the raw counts of the source and the raw counts of the background maps is used to calculate the detection maximum likelihood $L = -\ln(p)$.

3 SOURCE CATALOGUE

We cross-checked the detected sources of all observations/all EPICs with each other to obtain a final source catalogue. If

Table 1. *XMM-Newton* observations of Wil 1.

OBS-N0	OBS-ID	OBS-Date	EXP.T* (ks)		
			pn	MOS1	MOS2
1	0652810101	2010-10-22	14.1	22.5	22.4
2	0652810301	2010-10-25	20.6	27.8	27.5
3	0652810401	2010-10-31	26.5	32.3	32.7

*: Exposure time of EPICs after screening for high background.

Table 2. Offsets of the *XMM-Newton* observations

OBS-N0	EPIC	ΔRA (")	ΔDEC (")
1	PN	-0.33 ± 0.69	0.48 ± 0.69
	MOS1	-0.48 ± 0.83	-0.08 ± 0.83
	MOS2	-0.29 ± 0.63	0.29 ± 0.63
2	PN	-0.20 ± 0.54	0.53 ± 0.54
	MOS1	-0.02 ± 0.57	0.68 ± 0.57
	MOS2	-0.17 ± 0.52	0.32 ± 0.52
3	PN	0.16 ± 0.52	-0.49 ± 0.52
	MOS1	0.18 ± 0.64	-0.23 ± 0.64
	MOS2	0.33 ± 0.50	-0.01 ± 0.50

the positions of the sources in different observations/EPICs were closer than the 3σ statistical errors, we considered them as one source. The multiple *XMM-Newton* observations helped to remove the spurious sources caused by bad pixels, hot columns, gaps, edges of the CCD chips (Saxton et al. 2008). The final catalogue of 97 X-ray sources in the field of Wil 1 is listed in Table A1. The catalogue shows ID, right ascension (RA), declination (Dec), position uncertainty, and the flux of different observations for each source. The list of the sources are sorted using their coordinates. In this paper, each source is named by its ID, which is presented in Table A1.

For the astrometrical correction of the position of X-ray sources, we selected 11 X-ray sources, which had bright optical counterpart (apparent magnitude < 21 mag) and were already classified as AGNs in optical catalogues (see Sect. 4.3). The weighted mean of the ΔRA and the ΔDec between the positions of the optical and X-ray sources have been calculated to estimate the error of the position of X-ray sources for each observation (see Table 2). We found no significant instrumental shift in the RA and Dec of X-ray sources in none of the observations. Therefore, the coordinate and the positional error of each source were taken from the observation, in which the source was detected with the highest maximum likelihood.

To obtain the flux of the sources in each observation, we assumed an absorbed power law model with the Galactic foreground absorption in the direction of Wil 1 ($N_H = 1.17 \times 10^{20}$ cm $^{-2}$, HI4PI Collaboration et al. 2016) and a photon index of $\Gamma = 2$. The flux of the sources, for which spectral analysis was performed, are calculated using the best fit model to their spectrum (see Sect. 5.3). Table A1 shows the weighted flux of all EPICs measurements for each observation.

The mosaic image were created using the SAS task `emo-saicproc` out of the calibrated event files of all observations/EPICs. The task transforms the event files of different observations/pointings to a common image center, and after filtering the soft proton flares, it creates the exposure maps

(including vignetting), and the background maps and performs the source detection. Figure 1 shows the three-colour combined image of all observations. In Fig. 1, we show the main field of Wil 1 ($1r_h$) and also the regions of $3r_h$ and $5r_h$ of Wil 1.

4 CROSS-CORRELATION WITH OTHER CATALOGUES

We cross-correlated the X-ray source list with catalogues at other wavelengths. A source, which was located within the 3σ error circle of an X-ray source position, was considered to be its counterpart. We discuss the catalogues used in this work in the following.

4.1 Optical counterparts of X-ray sources

To study the optical counterparts of the X-ray sources, we have used the 11th and 12th released data of the Sloan Digital Sky Survey (Alam et al. 2015, SDSS12). The catalogue includes photometric data in the energy bands from the near ultraviolet (UV) to the near infrared ($u=3551$ Å, $g=4686$ Å, $r=6165$ Å, $i=7481$ Å, $z=8931$ Å) and allows a spectral study of the optical counterpart. For the u , g , r , i , and z bands, the Galactic extinction of 0.04, 0.03, 0.02, 0.01, and 0.01 mag is used in the direction of the Wil 1, respectively (Schlafly & Finkbeiner 2011). Table A2 presents the SDSS12 magnitudes of the optical counterparts of the X-ray sources. Figure 2 left image, shows the colour-magnitude diagram of the optical counterparts of the X-ray sources in the field of Wil 1. Logarithmic X-ray to optical flux ratio $\log(\frac{F_X}{F_{opt}})$, versus the X-ray flux and also hardness ratio (see Sect. 5.2) are plotted in Figure 3. The flux ratio $\log(\frac{F_X}{F_{opt}})$ was calculated using the equation of Maccacaro et al. (1988) modified for SDSS bands (Saeedi et al. 2016):

$$\log\left(\frac{F_X}{F_{opt}}\right) = \log_{10}(F_X) + \frac{g+r}{2 \times 2.5} + 5.37, \quad (1)$$

where F_X is the X-ray flux and g and r are the SDSS magnitudes of the optical counterpart associated with the X-ray source.

4.2 Infrared counterparts of X-ray sources

We searched for mid-infrared counterparts in the WISE All-Sky survey in four energy bands (3.4, 4.6, 12, and 22 μ m, named W1, W2, W3, and W4, respectively; Cutri & et al. 2014) and near-infrared counterparts in the 2MASS All-Sky Catalogue of Point Sources in the J , H , K bands (Cutri et al. 2003). The Galactic extinction for the infrared bands in the direction of Wil 1 was negligible (Schlafly & Finkbeiner 2011). Table A3 list the magnitudes of WISE and 2MASS counterparts of the X-ray sources. Figure 4 shows the colour-colour diagram of the WISE counterparts of the X-ray sources in the field of Wil 1. The colours are selected based on the study of Wright et al. (2010), which shows that many of background objects are expected to be red ($W2 - W3 > 1.5$) in WISE colour, while stars show ($W2 - W3 < 1.5$). In 2MASS near-infrared counterparts, background sources like e.g. AGNs and quasars are expected to

have $J-K > 1$ (see e.g. Masci et al. 2010). Only three sources had counterparts in the 2MASS near-infrared catalogue (see Table A3). These sources are classified as foreground star and galaxies as explained in Sect. 6.1 and Sect. 6.2.

4.3 Catalogues of AGNs and galaxies

Most of the background objects are AGNs. Many of these objects were already classified based on spectral properties in the optical and/or infrared surveys. The most updated optical/infrared catalogues of classified AGNs/quasars were considered in this work: The Million Quasars (Flesch 2019), WISE AGN candidates catalogs (Assef et al. 2018), QSOs selection from SDSS and WISE (Richards et al. 2015), and known quasars of the Gaia mission (Liao et al. 2019). In addition, we considered the catalogues, which classified galaxies: Vasconcellos et al. (2011) used the photometric data of SDSS7 (Abazajian et al. 2009) survey and separated the stars and galaxies based on a functional tree algorithm. We also used the more updated classification of Alam et al. (2015), which provides a classification of stars and galaxies using redshifts and colour criteria as the details are explained in Alam et al. (2015) and Ahn et al. (2012). The sources, which have been classified as AGNs or galaxies in above catalogues are labeled in Table A1.

4.4 Gaia and GALEX catalogues

To classify the foreground sources, we used the photometry and parallax measurement of the 2nd release of Gaia (Gaia Collaboration et al. 2018) and the GALEX catalogues of UV sources, which includes Galactic white dwarfs and hot stars (Bianchi et al. 2017).

5 X-RAY DATA ANALYSIS

We performed X-ray analysis for sources in the field of Wil 1. Following analyses were carried out for these sources.

5.1 X-ray timing analysis

To study the short-term variability of sources we have applied the Lomb-Scargle technique (Scargle 1982) and the pulsation Z_n^2 test (Buccheri et al. 1983, 1988). We extracted the light curves of bright sources (i.e. counts > 300 in each observation) in the energy range of 0.2–12 keV, and calculated their Lomb-Scargle periodograms. We could not find a signal of periodicity for any of the sources. In addition, we applied the Z_n^2 analysis for the barycentrically corrected event files of sources from each observation in the energy range of 0.2–12 keV and extracted the first and second harmonic periodograms. For none of the sources we found evidence for pulsation.

To study the long term variability, we checked the flux variation of sources over three XMM-Newton observations. Flux variation and its significance were calculated using

$$Var = \frac{F_{max}}{F_{min}} \text{ and } S = \frac{F_{max} - F_{min}}{\sqrt{EF_{max}^2 + EF_{min}^2}}, \quad (2)$$

respectively (Primini et al. 1993). F_{max} and F_{min} are the maximum and minimum X-ray flux, and EF_{min} and EF_{max}

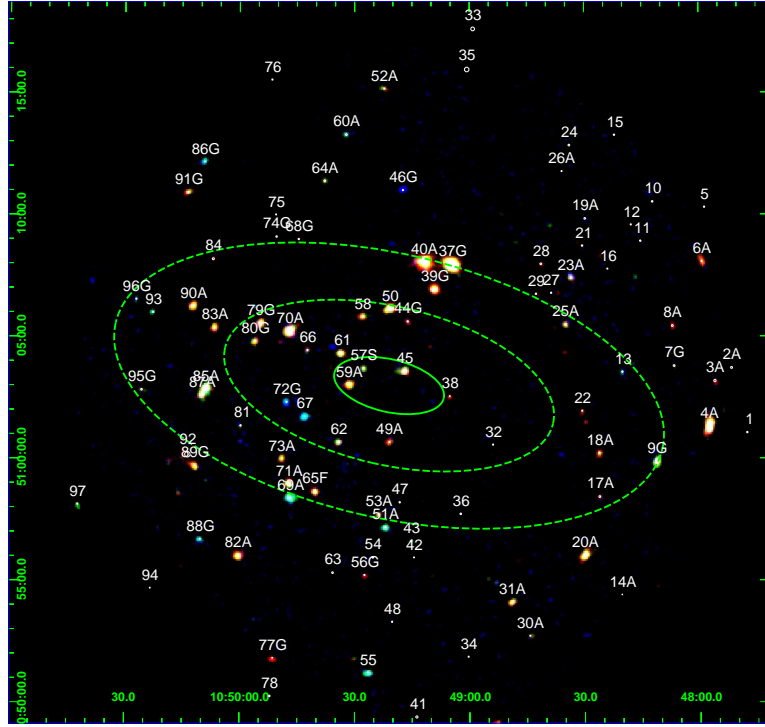


Figure 1. Combined X-ray image of *XMM-Newton* observations in the field of Wil 1 in the energy band of 0.2–12.0 keV. Green hard ellipse and dashed ellipses show 1, 3, and 5 half-light radii of Willman 1 dwarf galaxy, respectively. The colours red, green, blue present the energy ranges of 0.2–1.0 keV, 1.0–2.0 keV, and 2.0–12 keV, respectively. The images are smoothed with a 2D Gaussian with a kernel radius of 1.0 pixel. X-ray sources are marked with the source ID and the class of the sources (AGN: A, Galaxy: G, Foreground star: F, Symbiotic Star: S) in the final catalogue (Table A1).

are their corresponding errors. Due to the high background fluctuations, the energy band 5 (4.5–12.0 keV) was excluded in the calculation of the variability factor. The variability factor was calculated for the sources that were detected in at least two observations (see Table A1). The variability of a sources considered to be significant if S was higher than 3. Figure 5 shows the variability factor of the sources with significant variability. As it is shown in the plot, none of sources shows a very high variability during three *XMM-Newton* observations.

5.2 Hardness ratios

Hardness ratios (HRs) are useful parameters for the study of spectral properties of X-ray sources. The hardness ratio and its error are defined as

$$HR_i = \frac{B_{i+1} - B_i}{B_{i+1} + B_i} \text{ and } EHR_i = 2 \frac{\sqrt{(B_{i+1}EB_i)^2 + (B_iEB_{i+1})^2}}{(B_{i+1} + B_i)^2}, \quad (3)$$

respectively, where B_i is the count rate and EB_i is the corresponding error in the band i . For each source we calculated the hardness ratio of the observation, in which the source had the highest detection likelihood. In the next step, the hardness ratio is calculated only for those energy bands, which had a detection likelihood higher than 6 ($>3\sigma$). Table A1 shows the details of HRs for sources. Figure 6 shows the hardness ratio diagrams. We over-plotted the lines presenting the hardness ratios of different spectral models with various column densities from $N_H=10^{20} \text{ cm}^{-2}$

to $N_H=10^{23} \text{ cm}^{-2}$. We considered three power-law models with photon-index Γ of 1, 2, 3 for the hard sources, e.g, X-ray binaries, AGNs, or galaxies. Three *apec* model with the temperature of kT of 0.2, 1.0, and 2.0 keV correspond to the spectra of soft plasma emissions detected in different sources, e.g, supernova remnant (SNR), foreground stars, and symbiotic stars. The models, which describe the emission of the soft source (i.e, *apec* model with the temperature of kT of 0.2, 1.0) have a negligible rate in harder energy bands and therefore we do not have these models in *HR3* and *HR4*. Sources are classified as hard source when it has $HR2 - EHR2 > -0.2$, or only *HR3* and/or *HR4* are defined and there is no other classification for the source (Pietsch et al. 2005) (see Table A1).

5.3 X-ray spectral analysis

We extracted and analysed the X-ray spectra of bright sources in the field of Wil 1, which have not been classified as background objects (see Sect. 6). We extracted the spectra of the sources that had a net source counts of >500 in total. To improve the statistics of the spectrum of a source, we merged the spectra of all observations, in which the source was detected using the SAS task *epicspeccombine*. Before merging the spectra of different observation, we checked the variability of the source to exclude the spectrum of observation, in which the source showed a significantly different flux (see table A1). Figure 7 shows the spectrum of the X-ray sources and Table 3 the details of the models fitted to

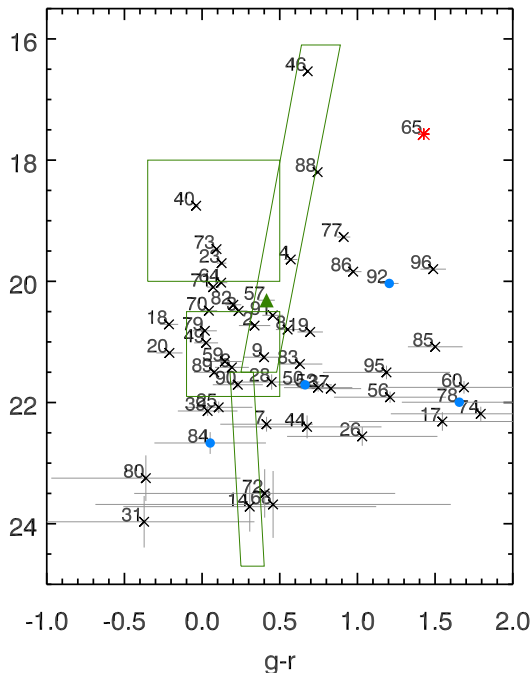


Figure 2. Colour-magnitude diagram (g versus $g-r$) for the SDSS12 optical counterparts of the X-ray sources. The green areas show the regions of the stellar isochrone of the Willman 1 dwarf galaxy according to Willman et al. (2011). In all plots classified background sources are marked by black cross, foreground stars by red asterisk, symbiotic stars by green triangle, and unclassified sources by blue circles.

the spectrum of sources. We fitted an absorbed power-law model or an absorbed collisionally-ionised thermal gas model (APEC, Brickhouse et al. 2000) to the spectrum of sources. The model for each source is selected based on the best fit. The details of the spectral study of each source are discussed in Sect. 6. For those sources, which were too faint for the spectral analysis, the hardness ratios can be used to characterise the spectrum of the sources (see Sect. 5.2).

6 CLASSIFICATION OF X-RAY SOURCES IN THE FIELD OF WIL 1

In following we explain the details of source classification in the field of Wil 1. Table 4 summarises the criteria of the source classification.

6.1 Classified AGN and galaxies

As Figure 4 shows, sources, which have been classified as background galaxies or AGNs (see Table. A1) show consistency with the properties of background objects in deep infrared studies as explained in Sect. 4.2. Only sources No. 46 and No. 88 have a 2MASS near-infrared counterpart, which has a similar colour of background sources in 2MASS survey (see Sect. 4.2). These two sources are the brightest background galaxies in the field of Wil 1 and their extent is visu-

ally observable in their optical counterpart (see Fig. 8). The classified background sources with optical counterpart have X-ray to optical flux ratio $\log\left(\frac{F_x}{F_{opt}}\right) > -1.0$ (see Fig. 3). It is also similar to the ratio of background sources in other studies (see e.g. Ducci et al. 2013; Saeedi et al. 2016). As Fig. 3 shows, for the majority of background sources the X-ray emission is more dominant than the optical emission, which is different from foreground stars or symbiotic stars. The HR diagrams of Fig. 6 show that most of the classified background sources have a hard spectrum (located in the area of power-law models with $\Gamma=1, 2$).

6.2 Sources No. 65, a foreground M dwarf

Source No. 65 has optical and infrared counterparts with $W2 - W3 < 2$, $J - K < 1$, and $\log\left(\frac{F_x}{F_{opt}}\right) < 0$. This makes its classification as a foreground star likely (Saeedi et al. 2016; Ducci et al. 2013; Salvato et al. 2018). The optical and infrared colours of the source with $g - r = 1.40 \pm 0.01$, $r - i = 0.98 \pm 0.01$, $r - z = 0.52 \pm 0.01$, and $z - J = 1.29 \pm 0.05$, $J - H = 0.57 \pm 0.09$, and $H - K_s = 0.28 \pm 0.09$ agree very well with the M dwarfs of the spectral type M2 according to West et al. (2011). It is located at the distance of 437^{+34}_{-30} pc based on the parallax measurement of Bailer-Jones et al. (2018)¹. The spectrum of the source is fitted with an absorbed apec model (see Table 3 and Fig. 7) with a temperature of $kT = 2.97^{+2.33}_{-1.20}$ keV, which is slightly higher than the typical temperature of classified M dwarfs in the field of Draco dSph (Saeedi et al. 2019). The flux of the source stays at similar values over the three XMM-Newton observations. In addition, the individual light curve of each observation shows no flare activity. The X-ray luminosity of the order 10^{29} erg s⁻¹ is consistent with an M2 dwarf with an age of ~ 0.01 Gyr (see Stelzer et al. 2013).

6.3 Source No. 57, symbiotic star in the Wil 1 dSph

This source is located in the central region of the Wil 1. Figure 9 shows the 3σ error circle of the X-ray source position in observation 3, where source No. 57 had the highest detection likelihood. Within this error circle position the source No. 57 has an optical counterpart, which is located in the red giant branch of the Wil 1 sources (see Fig. 2). In addition, this optical counterpart is classified as a member of the Wil 1 by Martin et al. (2007) with a radial velocity of -11.7 ± 2.8 km s⁻¹ and a metallicity of $[\text{Fe}/\text{H}] = -1.6$, which both are in a very good agreement with the systemic velocity (-12.8 ± 1.0 km s⁻¹) and the low metallicity of Wil 1 members (Martin et al. 2007; Willman et al. 2011). The source has $\log\left(\frac{F_x}{F_{opt}}\right) \leq 0$, similar to stellar objects classified by Saeedi et al. (2019) in Draco dSph. Its X-ray spectrum is fitted well with an absorbed apec model (see Table 3 and Fig. 7 upper right). The temperature of the source of $kT = 3.60^{+9.59}_{-2.12}$ keV is similar to the temperature of the β -type symbiotic (Luna et al. 2013; Saeedi et al. 2019). The column density of the source is higher than the Galactic absorption

¹ Gaia source ID: 835973362206830080

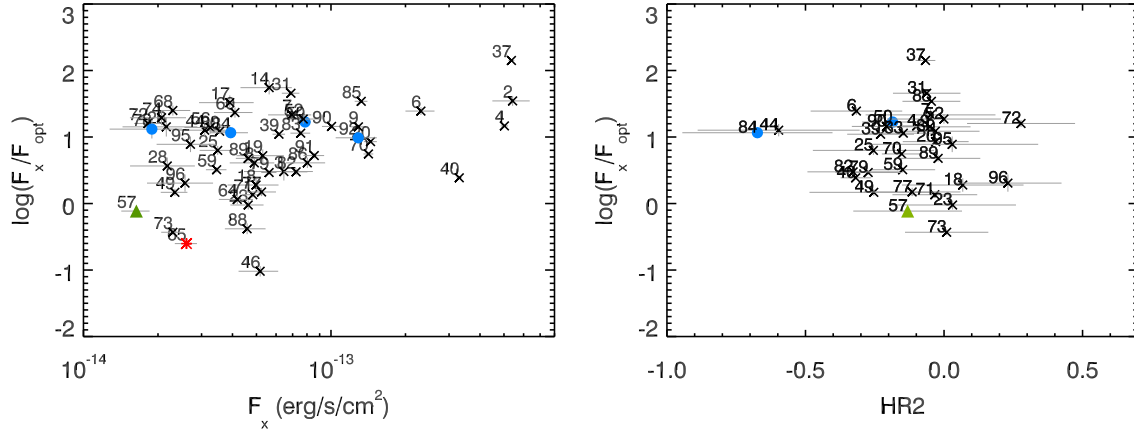


Figure 3. Logarithmic X-ray to optical flux ratio $\log(\frac{F_X}{F_{\text{opt}}})$ versus the maximum X-ray flux (**left**) and HR2 (**right**). The symbols are the same as Fig. 2.

Table 3. Best-fit parameters of the X-ray spectra. Errors are at the 90% confidence level.

Src-No	Model	N_{H} 10^{22} cm^{-2}	Photon index	kT keV	Abundance	χ^2 (d.o.f)	Absorbed F_{X} $10^{-15} \text{ erg s}^{-1} \text{ cm}^{-2}$	$L_{\mathrm{X}}^{(1)}$ erg s^{-1}
45	tbabs×(po)	<0.13	$2.00^{+0.46}_{-0.32}$			1.07 (39)	$21.48^{+2.83}_{-2.82}$	4.1×10^{33}
50 ⁽²⁾	tbabs×(apec+apec)	<0.06		$kT1=0.17^{+0.10}_{-0.12}$	<0.18	1.35 (44)	$41.49^{+3.96}_{-3.94}$	7.9×10^{33}
				$kT2=5.27^{+3.53}_{-1.62}$				
57 ⁽³⁾	tbabs×tbabs(apec)	$N_{\mathrm{H}}1=0.012$ frozen $N_{\mathrm{H}}2=0.14^{+0.17}_{-0.09}$		$3.60^{+9.59}_{-2.12}$	<1.0	1.10 (10)	$10.43^{+2.31}_{-8.07}$	2.0×10^{33}
58	tbabs×(apec)	<0.06		$1.71^{+1.21}_{-0.73}$	<0.90	0.91 (9)	$6.80^{+1.30}_{-1.38}$	1.6×10^{33}
61	tbabs×(apec)	$0.04^{+0.05}_{-0.03}$		$4.36^{+4.96}_{-1.84}$	<1.01	1.07 (30)	$20.7^{+2.71}_{-2.76}$	4.0×10^{33}
65	tbabs×(apec)	<0.02		$2.97^{+2.33}_{-1.20}$	<0.22	1.13 (26)	$10.33^{+1.93}_{-3.85}$	$3.3 \times 10^{29(4)}$
66	tbabs×(po)	<0.58	$2.49^{+2.55}_{-1.05}$			1.86 (5)	$4.45^{+2.72}_{-1.92}$	8.5×10^{32}
67	tbabs×(po)	$0.54^{+0.45}_{-0.31}$	$1.34^{+0.54}_{-0.47}$			1.02 (16)	$45.71^{+11.50}_{-8.72}$	8.7×10^{33}

(1): We assumed a distance of Wil 1 (~ 40 kpc) to estimate the luminosity of the sources (see Sect. 1).

(2): For the source No. 50 there are two temperatures of two `apec` models: $kT1$ and $kT2$.

(3): Source No.57 has two absorption models, which show the Galactic absorption(N_{H1}) and the intrinsic absorption (N_{H2}).

(4): For the source No. 65, which is classified as a foreground M dwarf, the distance of 441 parsec is taken to estimate its luminosity (see Sect. 6).

Table 4. Summary of critria of source classification in field of Wil 1.

source type	classification critera
foreground stars	$\log(\frac{F_X}{F_{\text{opt}}}) < 0$, infrared counterpart with $W2 - W3 < 1.5$ and/or $J - K < 1$, optical counterpart brighter or redder (M dwarfs) than the stellar isochrone of Wil 1, main X-ray emission < 2.0 keV
AGNs	$-1 < \log(\frac{F_X}{F_{\text{opt}}}) < 2$, infrared counterpart with $W2 - W3 > 1.5$ and/or $J - K > 1$, $HR2 > -0.5$
galaxies	$-1 < \log(\frac{F_X}{F_{\text{opt}}}) < 2$, infrared counterpart with $W2 - W3 > 1.5$ and/or $J - K > 1$, optically classified as a galaxy.
symbiotic stars	$\log(\frac{F_X}{F_{\text{opt}}}) < 0$, infrared counterpart of an stellar object ($W2 - W3 < 1.5$) and optical counterpart on the isochrone of Wil 1 dSph or confirmed as member of Wil 1 dSph, X-ray emmsion similar to one of the types of symbiotic stars (Luna et al. 2013)
hard sources	$HR2 - EHR2 > -0.2$, or only $HR3$ and/or $HR4$ are defined

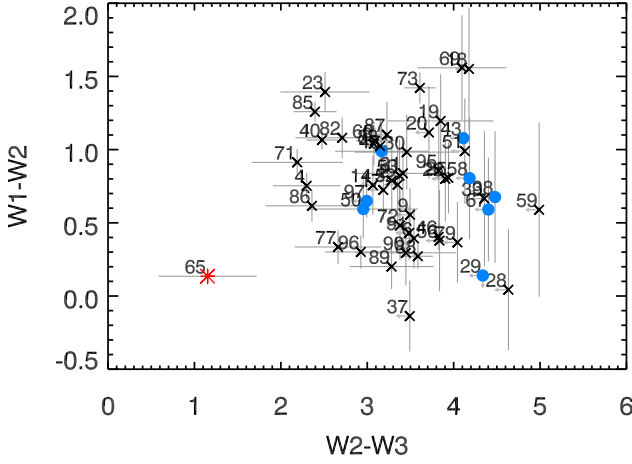


Figure 4. Colour-colour diagram of mid-infrared WISE (W1(3.4 μm) – W2(4.6 μm) versus (W2(4.6 μm) – W3(12 μm)). Arrows show instead of error bars for the sources, which have upper limits in the WISE bands (see Table A3). The symbols are the same as Fig. 2.

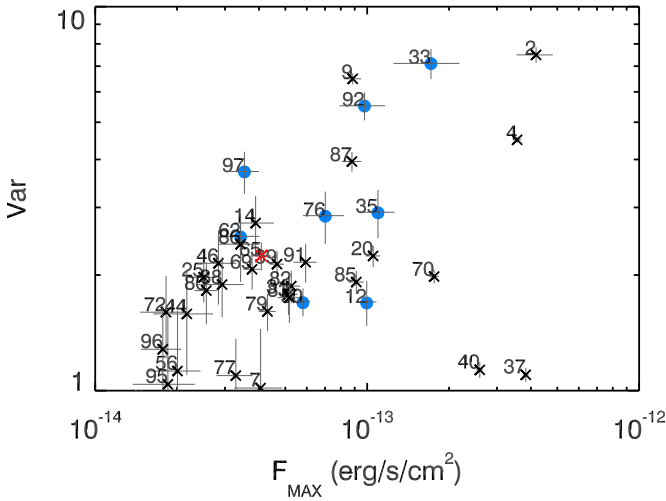


Figure 5. Variability factor of sources with significant variability ($S>3$) in the energy band of 0.2–4.5 keV plotted versus the maximum flux. The symbols are the same as Fig. 2.

in the direction of Wil 1 ($N_{\text{H}}=1.17\times 10^{20} \text{ cm}^{-2}$). We assumed two absorption model for the source: a Galactic absorption, frozen to the N_{H} in the direction of Wil 1, and the intrinsic absorption of $N_{\text{H}}=0.14^{+0.17}_{-0.09}\times 10^{22} \text{ cm}^{-2}$ for the source itself, which can be related to colliding winds region of the symbiotic star (Luna et al. 2013). We classify this source as a symbiotic star in Wil 1.

6.4 Sources with optical counterpart

Only sources No. 50, 78, 84 and 92 are unclassified X-ray sources with an optical counterpart (see Fig. 2). Their opti-

cal counterpart is classified as a stellar object in SDSS12 survey (Alam et al. 2015). Among these four source only source No. 50 has a WISE infrared counterpart too (see Fig. 4).

Sources No. 50, 84: The optical counterpart of these two sources can be a main sequence star in Wil 1 (see Fig. 2). The X-ray spectrum of source No. 50 is fitted with an absorbed *apec* model with two components (see Fig. 7 and Table 3). The absorption of the source is consistent with the Galactic absorption towards Wil 1 and the abundance of the source is consistent with the low metallicity of Wil 1 members. The HR of source No. 84 shows that the main emission of the source is $<2 \text{ keV}$ (see Table A1) and it has a softer emission in comparison to the known background sources (see Fig. 6 and 3). As Fig. 3 shows both sources have $\log(\frac{F_{\text{X}}}{F_{\text{opt}}}) > 1$. Assuming that source No. 50 and No. 84 are located at the distance of Wil 1 ($\sim 40 \text{ kpc}$), their luminosities are $\sim 7.9\times 10^{33}$ and $2.0\times 10^{33} \text{ erg s}^{-1}$, respectively.

In the following, we discuss about the possibilities of these two sources being candidates for either cataclysmic variables (CVs, i.e. accreting white dwarf with a main sequence companion), or low mass X-ray binaries (LMXBs). The X-ray emission in CVs depends on the strength of the magnetic field of the white dwarf and the accretion rate. There are two main classes of magnetic and non-magnetic CVs. In non-magnetic CVs an accretion disk can form around the white dwarf. The disk -itself- is not hot enough to emit X-rays. However, if the boundary layer between the disk and surface of the white dwarf is optically thin, X-ray emission can be produced. In this case the X-ray emission is hard with a corresponding temperature of a few keV and an X-ray luminosity between 10^{29} – $10^{32} \text{ erg s}^{-1}$ (Mukai 2017; Kuulkers et al. 2006). If the system undergoes the nova eruption, the boundary layer becomes optically thick, therefore the system shows a soft X-ray emission of 0.1–0.5 keV and higher luminosities (Mukai 2017). Magnetic CVs have two sub-classes of polars (with strong magnetic field) and intermediate polars (with weakly magnetic white dwarf). Polars have no accretion disk and materials follows the magnetic lines to reach to the surface of the white dwarf. Polars are characterised by a dominant soft X-ray emission and a bolometric luminosity of $\sim 10^{32} \text{ erg s}^{-1}$ (Mukai 2017). There are cases, in which polars show emission up to $\sim 10 \text{ keV}$, however, in these cases the bolometric luminosity decreases around two orders of magnitude (e.g. Ramsay et al. 2004). In case of intermediate polars, a truncated accretion disk can form. The attachment of the inner part of the accretion disk with the magnetic field of white dwarf forms accretion curtains above the poles of the white dwarfs, where the materials experience strong shocks, and therefore, a hard X-ray emission of 5–50 keV, with a X-ray luminosity up to a few $10^{33} \text{ erg s}^{-1}$ is produced (Mukai 2017; Balman 2012). Fluorescent Fe $K\alpha$ lines were observed in most of the intermediate polars (Kuulkers et al. 2006). On the basis of the samples of Mukai (2017), CVs have a $\log(\frac{F_{\text{X}}}{F_{\text{opt}}}) < 1.0$ and magnetic CVs generally have a $\log(\frac{F_{\text{X}}}{F_{\text{opt}}})$ larger than that of non-magnetic CVs. According the above characteristics of spectrum and luminosity of different types of the CVs, source No. 50 and No. 84 do not fit to any class of them.

On the other hand, The low luminosity of the sources suggests that they are no persistent LMXBs, which normally have X-ray luminosities $> 10^{35} \text{ erg s}^{-1}$. However, they

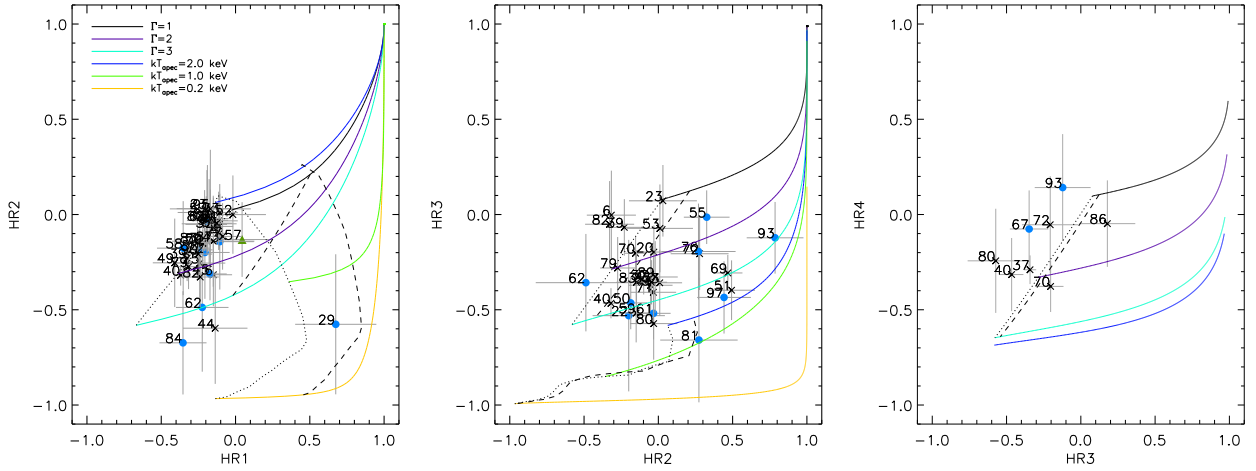


Figure 6. Hardness ratio diagrams. The plotted hard lines are the hardness ratios calculated for different spectral models and column densities. The column densities of $N_{\text{H}}=10^{20} \text{ cm}^{-2}$ (dotted lines) and $N_{\text{H}}=10^{21} \text{ cm}^{-2}$ (dashed lines) are plotted for the power-law models and apec models. The symbols are the same as Fig. 2.

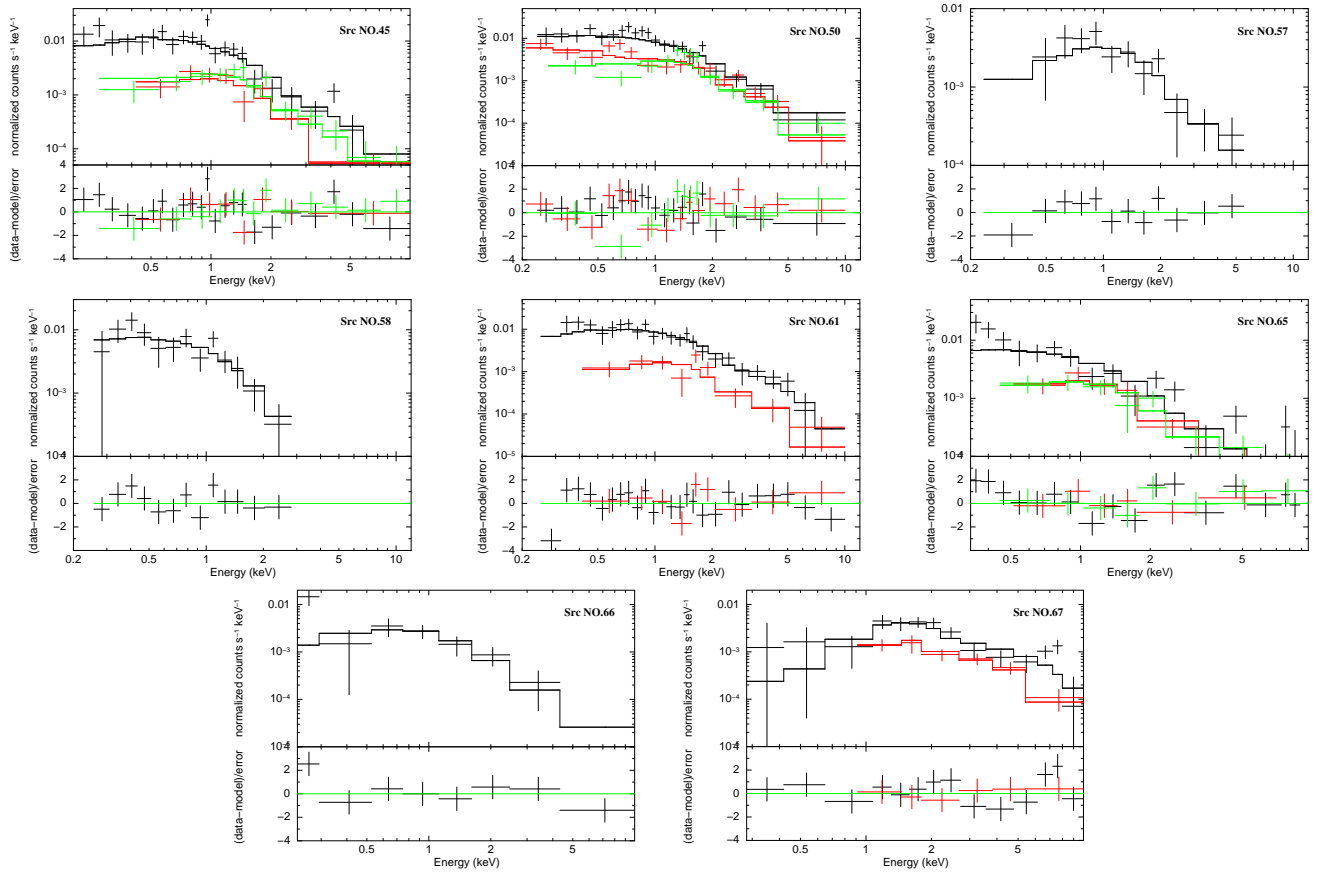


Figure 7. Combined spectrum of all *XMM-Newton* observations of sources in the FOV of Willman 1 dSph, which have enough statistics for spectral analysis: EPIC-pn (black), EPIC-MOS1 (red), and EPIC-MOS2 (green), together with the residuals in units of the standard deviation.

might be transient LMXBs. Observational studies show that transient LMXBs are low luminosity X-ray sources ($\sim 10^{31} - 10^{33} \text{ erg s}^{-1}$) with soft X-ray emissions ($< 5.0 \text{ keV}$) (e.g, Yokogawa et al. 2000; Campana et al. 1998). The models behinds these very faint accretors are explained in the

work of e.g, King & Wijnands (2006). Simulations predict that transient LMXBs are common X-ray sources in galaxies and can be observed several million years after the star formation (Bogomazov & Lipunov 2008; van Haaften et al. 2015). Sources No. 50 and 84 show no pulsation. Also, their

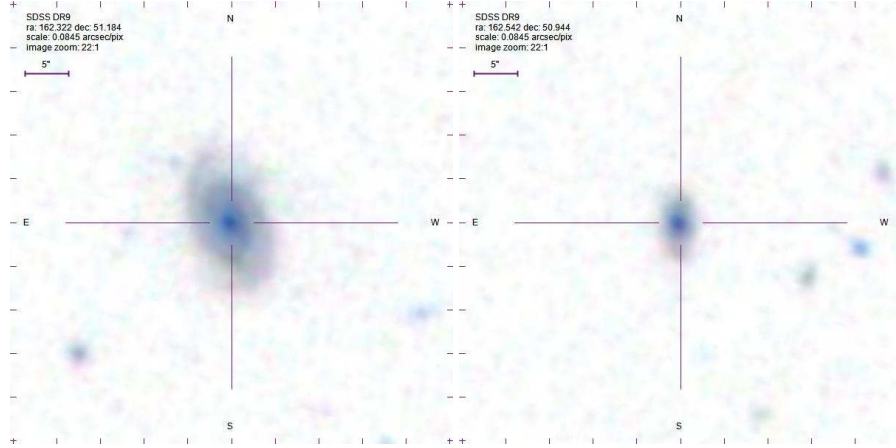


Figure 8. Optical SDSS9 image of counterparts of sources No. 46 (Left) and No. 88 (right), which are classified as background galaxies.

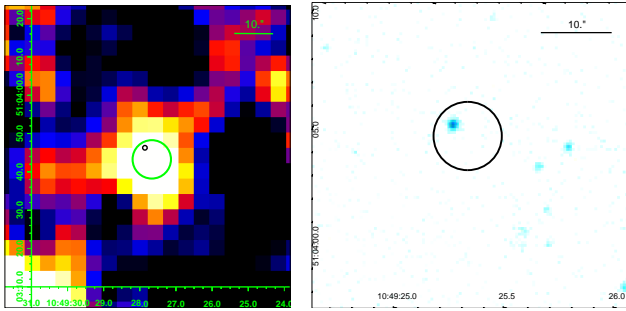


Figure 9. Left: X-ray mosaic image of Source No. 57 in the energy range of 0.2–12.0 keV. The green circle shows the 3σ X-ray position of the source and the black circle shows the position of the optical counterpart. Right: Optical SDSS9 image of the stellar counterpart of source No. 57. Black region shows the 3σ position of the X-ray source.

optical counterparts are not confirmed as Wil 1 members in the studies of [Martin et al. \(2007\)](#) and [Willman et al. \(2011\)](#). Therefore, these sources remain unclassified being, either transient LMXBs or background objects.

Sources No. 78, 92: Source No. 92 is a variable source (see Fig. 5). X-ray to optical flux ratio of both sources are $\log(\frac{F_X}{F_{opt}}) > 1$. The position of the optical counterparts of these two sources in the colour-magnitude diagram (see Fig. 2) and also the location of them (out of the $5r_h$ of the field of Wil 1; see Fig. 1 and Sect. 1) make them rather unlikely members of Wil 1.

6.5 Sources with WISE infrared counterpart

Sources **No. 29, 38, 43, 45, 58, 67, 97** have only an infrared counterpart in WISE survey, and no optical counterpart is found for these sources. The position of all these sources in colour-colour WISE diagram shows that they all have infrared colours similar to the background objects (see Fig. 4). The spectral analysis of source No. 45 and 67 (see Fig. 7 and Table. 3) shows that an absorbed **power-law** model is fitted to the spectrum of these two sources. Source No. 97 is also a hard variable source (see Table A1, and Fig. 5). Source No. 97 and also 43, which is located outside

of the $5r_h$ of the main field of Wil 1 can be candidate for a background source. However, in case of sources No. 45, and 67 the classification needs more criteria, since they can be the members of Wil 1.

Source No. 58 has a soft X-ray spectrum. An absorbed **apex** model with a temperature of ~ 1.4 keV (see table. 3 and Fig. 7) is fitted to the spectrum. For the sources No. 29, 38 the HRs show that their main emission is observed < 2 keV. They remain unclassified since there is not enough information for their classification.

6.6 Sources without counterpart

The rest of the X-ray sources in the field of Wil 1 have no optical/infrared counterparts. Among them, sources **No. 22, 55, 61, 62, 76, 81, 93** are classified as hard X-ray sources using the HRs criteria (see Sect. 5.2). Also, source No. 22, 61, 62, 66, 81, 93 are located within the $5r_h$ of Wil 1. For sources **61, 66** we have performed a spectral analysis. An absorbed **power-law** model is fitted to the spectrum of source No. 61. As for source No. 66, poor statistics of the spectrum do not allow to determine a significant temperature for the source. Since there is no optical/infrared counterpart for these sources, no advanced classification is possible for them.

7 SUMMARY

We have detected and performed a classification of X-ray sources in the field of Wil 1 using three *XMM-Newton* observations and multi-wavelength studies. Our study shows that most of the X-ray sources in the field of Wil 1 are background galaxies and AGNs. This result is consistent with the results, which have been obtained for other dSphs (e.g. [Manni et al. 2015](#); [Saeedi et al. 2016](#); [Maccarone et al. 2005](#)). Only one foreground star (M dwarf) is detected in the field of Wil 1. Also, we classified a symbiotic star in Wil 1. This is consistent with the result of our recent deep X-ray study of the Draco dSph ([Saeedi et al. 2019](#)) and confirms the detection of accreting white dwarfs in these old population of dSphs. Moreover, eleven sources are classified as hard sources in the field of Wil 1.

We could not confirm the presence of any LMXB in Wil 1. So

far, no LMXBs have been detected in nearby dSph. However, theoretically, transient LMXBs can exist for a long time in galaxies and be detectable as soft and low luminosity X-ray sources. Additional X-ray studies of different nearby dSphs with different age, star formation, and distance are necessary to verify the existence of LMXBs in dSphs.

ACKNOWLEDGEMENTS

This research was funded by the DLR research grant BWVI/DLR 500R1907 and DFG SA 2131/12-1. This study is based on observations obtained with *XMM-Newton*, an ESA science mission with instruments and contributions directly funded by ESA Member States and NASA. This research has made use of the SIMBAD and VIZIER database, operated at CDS, Strasbourg, France, and of the NASA/IPAC Extragalactic Database (NED), which is operated by the Jet Propulsion Laboratory, California Institute of Technology, under contract with the National Aeronautics and Space Administration. This publication makes use of data products from the Wide field Infrared Survey Explorer, which is a joint project of the University of California, Los Angeles, and the Jet Propulsion Laboratory/California Institute of Technology, funded by the National Aeronautics and Space Administration. This publication has made use of data products from the Two Micron All Sky Survey, which is a joint project of the University of Massachusetts and the Infrared Processing and Analysis Center, funded by the National Aeronautics and Space Administration and the National Science Foundation. Funding for SDSS and SDSS-III has been provided by the Alfred P. Sloan Foundation, the Participating Institutions, the National Science Foundation, and the US Department of Energy Office of Science. The SDSS-III web site is <http://www.sdss3.org/>. SDSS-III is managed by the Astrophysical Research Consortium for the Participating Institutions of the SDSS-III Collaboration including the University of Arizona, the Brazilian Participation Group, Brookhaven National Laboratory, University of Cambridge, University of Florida, the French Participation Group, the German Participation Group, the Instituto de Astrofísica de Canarias, the Michigan State/Notre Dame/JINA Participation Group, Johns Hopkins University, Lawrence Berkeley National Laboratory, Max Planck Institute for Astrophysics, New Mexico State University, New York University, Ohio State University, Pennsylvania State University, University of Portsmouth, Princeton University, the Spanish Participation Group, University of Tokyo, University of Utah, Vanderbilt University, University of Virginia, University of Washington, and Yale University. This research has made use of SAO Image DS9, developed by Smithsonian Astrophysical Observatory.

REFERENCES

- Abazajian K. N., et al., 2009, *ApJS*, **182**, 543
- Ahn C. P., et al., 2012, *ApJS*, **203**, 21
- Alam S., et al., 2015, *ApJS*, **219**, 12
- Arnason R. M., Barmby P., Bahramian A., Maccarone T. J., Zepf S. E., 2019, *MNRAS*, **485**, 2259
- Assef R. J., Stern D., Noirot G., Jun H. D., Cutri R. M., Eisenhardt P. R. M., 2018, *ApJS*, **234**, 23
- Bailer-Jones C. A. L., Rybizki J., Foesneau M., Mantelet G., Andrae R., 2018, *AJ*, **156**, 58
- Balman S., 2012, *Mem. Soc. Astron. Italiana*, **83**, 585
- Bianchi L., Shiao B., Thilker D., 2017, *ApJS*, **230**, 24
- Bogomazov A. I., Lipunov V. M., 2008, *Astronomy Reports*, **52**, 299
- Brickhouse N. S., Smith R. K., Raymond J. C., Liedahl D. A., 2000, in *AAS/High Energy Astrophysics Division #5*. p. 27.01
- Buccheri R., et al., 1983, *A&A*, **128**, 245
- Buccheri R., di Gesu V., Maccarone M. C., Sacco B., 1988, *A&A*, **201**, 194
- Campana S., Colpi M., Mereghetti S., Stella L., Tavani M., 1998, *A&ARv*, **8**, 279
- Cutri R. M., et al. 2014, *VizieR Online Data Catalog*, [p. II/328](#)
- Cutri R. M., et al., 2003, *VizieR Online Data Catalog*, [p. II/246](#)
- Ducci L., Sasaki M., Haberl F., Pietsch W., 2013, *A&A*, **553**, A7
- Fabbiano G., 2006, *ARA&A*, **44**, 323
- Flesch E. W., 2019, *VizieR Online Data Catalog*, [p. VII/283](#)
- Gaia Collaboration et al., 2018, *A&A*, **616**, A1
- HI4PI Collaboration et al., 2016, *A&A*, **594**, A116
- King A. R., Wijnands R., 2006, *MNRAS*, **366**, L31
- Kuulkers E., Norton A., Schwope A., Warner B., 2006, X-rays from cataclysmic variables. pp 421–460
- Liao S.-L., Qi Z.-X., Guo S.-F., Cao Z.-H., 2019, *Research in Astronomy and Astrophysics*, **19**, 029
- Loewenstein M., Kusenko A., 2012, *ApJ*, **751**, 82
- Luna G. J. M., Sokolowski J. L., Mukai K., Nelson T., 2013, *A&A*, **559**, A6
- Maccarone T., Gioia I. M., Wolter A., Zamorani G., Stocke J. T., 1988, *ApJ*, **326**, 680
- Maccarone T. J., Kundu A., Zepf S. E., Piro A. L., Bildsten L., 2005, *MNRAS*, **364**, L61
- Manni L., Nucita A., De Paolis F., 2014, in *The X-ray Universe 2014*. p. 280
- Manni L., Nucita A. A., De Paolis F., Testa V., Ingrosso G., 2015, *MNRAS*, **451**, 2735
- Martin N. F., Ibata R. A., Chapman S. C., Irwin M., Lewis G. F., 2007, *MNRAS*, **380**, 281
- Masci F. J., Cutri R. M., Francis P. J., Nelson B. O., Huchra J. P., Heath Jones D., Colless M., Saunders W., 2010, *Publ. Astron. Soc. Australia*, **27**, 302
- McConnachie A. W., 2012, *AJ*, **144**, 4
- Mukai K., 2017, *PASP*, **129**, 062001
- Pietsch W., Freyberg M., Haberl F., 2005, *A&A*, **434**, 483
- Primini F. A., Forman W., Jones C., 1993, *ApJ*, **410**, 615
- Ramsay G., Wu K., 2006, *A&A*, **459**, 777
- Ramsay G., Cropper M., Wu K., Mason K. O., Córdova F. A., Priedhorsky W., 2004, *MNRAS*, **350**, 1373
- Richards G. T., et al., 2015, *ApJS*, **219**, 39
- Saeedi S., Sasaki M., Ducci L., 2016, *A&A*, **586**, A64
- Saeedi S., Sasaki M., Stelzer B., Ducci L., 2019, *A&A*, **627**, A128
- Salvato M., et al., 2018, *MNRAS*, **473**, 4937
- Saxton R. D., Read A. M., Esquej P., Freyberg M. J., Altieri B., Bermejo D., 2008, *A&A*, **480**, 611
- Scargle J. D., 1982, *ApJ*, **263**, 835
- Schlafly E. F., Finkbeiner D. P., 2011, *ApJ*, **737**, 103
- Stelzer B., Marino A., Micela G., López-Santiago J., Liefke C., 2013, *MNRAS*, **431**, 2063
- Strüder L., et al., 2001, *A&A*, **365**, L18
- Tolstoy E., Hill V., Tosi M., 2009, *ARA&A*, **47**, 371
- Turner M. J. L., et al., 2001, *A&A*, **365**, L27
- Vasconcellos E. C., de Carvalho R. R., Gal R. R., LaBarbera F. L., Capelato H. V., Frago Campos Velho H., Trevisan M., Ruiz R. S. R., 2011, *AJ*, **141**, 189
- Weisz D. R., Dolphin A. E., Skillman E. D., Holtzman J., Gilbert K. M., Dalcanton J. J., Williams B. F., 2014, *ApJ*, **789**, 147
- West A. A., et al., 2011, *AJ*, **141**, 97
- Willman B., et al., 2005, *AJ*, **129**, 2692
- Willman B., Geha M., Strader J., Strigari L. E., Simon J. D., Kirby E., Ho N., Warren A., 2011, *AJ*, **142**, 128
- Wright E. L., et al., 2010, *AJ*, **140**, 1868
- Yokogawa J., Paul B., Ozaki M., Nagase F., Chakrabarty D., Takeshima T., 2000, *ApJ*, **539**, 191
- van Haften L. M., Nelemans G., Voss R., van der Sluis M. V., Toonen S., 2015, *A&A*, **579**, A33

APPENDIX A: SOURCE CATALOGUE

Table A1: X-ray sources in the FOV of Willman 1 dSph.

Src-NO	RA (J2000)	DEC (J2000)	r1 σ (")	Flux* ** (0.2–12. keV) (10 ⁻¹³ erg s ⁻¹ cm ⁻²)			Hardness ratio				Var	Classification [†]
				OBS1	OBS2	OBS3	HR1	HR2	HR3	HR4		
1	10 47 47.61	+51 01 03.3	1.73	0.61 ± 0.20	N	0.75 ± 0.15	–	–	–	–	1.24 ± 0.47	
2	10 47 51.63	+51 03 42.6	2.35	5.42 ± 0.93	N	0.91 ± 0.22	-0.44 ± 0.17	–	–	–	7.48 ± 0.35	AGN ^{2,5,6}
3	10 47 55.99	+51 03 10.4	2.85	N	0.65 ± 0.20	0.40 ± 0.09	–	–	–	–	1.05 ± 0.43	AGN ^{1,4}
4	10 47 57.51	+51 01 20.9	0.40	3.46 ± 0.19	4.02 ± 0.17	5.02 ± 0.17	-0.11 ± 0.04	-0.09 ± 0.05	-0.35 ± 0.06	–	4.49 ± 0.08	AGN ^{2,5,6}
5	10 47 58.61	+51 10 18.3	1.60	0.58 ± 0.22	N	N	–	–	–	–	–	
6	10 47 59.34	+51 08 04.5	1.09	1.85 ± 0.36	2.31 ± 0.31	1.36 ± 0.22	-0.14 ± 0.12	-0.31 ± 0.16	0.00 ± 0.23	–	1.54 ± 0.25	AGN ^{1,4}
7	10 48 06.61	+51 03 47.7	2.10	<16.40	0.54 ± 0.11	0.69 ± 0.13	-0.18 ± 0.18	-0.05 ± 0.23	–	–	1.00 ± 0.43	galaxy ⁶
8	10 48 07.04	+51 05 26.2	2.22	0.49 ± 0.10	0.30 ± 0.06	0.46 ± 0.11	-0.38 ± 0.19	–	–	–	2.46 ± 0.44	AGN ^{1,2,3,4}
9	10 48 11.30	+50 59 52.7	1.26	1.03 ± 0.10	1.29 ± 0.09	1.21 ± 0.11	-0.19 ± 0.14	-0.051 ± 0.14	-0.37 ± 0.16	–	6.47 ± 0.21	galaxy ⁶
10	10 48 12.18	+51 10 31.9	1.96	0.83 ± 0.26	<12.96	<10.32	–	–	–	–	–	
11	10 48 15.33	+51 08 55.3	1.77	<14.62	<11.24	0.56 ± 0.13	–	–	–	–	–	
12	10 48 17.79	+51 09 35.4	1.42	<11.18	1.29 ± 0.14	0.90 ± 0.16	–	–	–	–	1.69 ± 0.22	
13	10 48 20.12	+51 03 33.4	1.75	N	0.29 ± 0.08	0.30 ± 0.07	–	–	–	–	1.04 ± 0.49	
14	10 48 20.30	+50 54 20.6	0.85	N	0.56 ± 0.13	0.25 ± 0.09	-0.08 ± 0.31	–	–	–	2.72 ± 0.48	AGN ²
15	10 48 22.11	+51 13 16.1	1.71	0.52 ± 0.17	1.12 ± 0.22	<8.54	–	–	–	–	1.54 ± 0.41	
16	10 48 23.95	+51 07 46.9	1.37	0.68 ± 0.13	<9.21	<7.86	–	–	–	–	–	
17	10 48 26.11	+50 58 26.2	2.22	<10.13	0.39 ± 0.10	N	–	–	–	–	–	AGN ²
18	10 48 26.17	+51 00 14.3	1.63	0.50 ± 0.12	0.27 ± 0.04	0.30 ± 0.06	–	0.06 ± 0.22	–	–	1.80 ± 0.35	AGN ^{1,2,3,4}
19	10 48 29.82	+51 09 50.6	1.98	<10.56	0.53 ± 0.11	0.43 ± 0.10	-0.41 ± 0.16	–	–	–	1.01 ± 0.43	AGN ^{1,2,3,4}
20	10 48 29.97	+50 56 03.6	0.89	1.40 ± 0.10	1.45 ± 0.09	1.15 ± 0.10	-0.15 ± 0.09	-0.03 ± 0.11	-0.19 ± 0.13	–	2.23 ± 0.14	AGN ^{1,2,3,4}
21	10 48 30.55	+51 08 43.9	1.78	0.52 ± 0.12	N	<6.45	–	–	–	–	–	
22	10 48 30.62	+51 01 57.7	1.43	0.33 ± 0.06	<7.13	0.40 ± 0.07	-0.20 ± 0.16	-0.19 ± 0.24	-0.53 ± 0.39	–	1.10 ± 0.33	Hard source
23	10 48 33.50	+51 07 25.1	1.00	0.46 ± 0.07	0.36 ± 0.05	0.42 ± 0.05	-0.18 ± 0.20	0.03 ± 0.22	0.07 ± 0.18	–	1.54 ± 0.26	AGN ^{1,2,3,4}
24	10 48 33.93	+51 12 51.0	2.11	<13.69	<6.45	0.52 ± 0.10	–	–	–	–	–	
25	10 48 34.91	+51 05 30.1	1.27	0.35 ± 0.05	0.33 ± 0.05	0.34 ± 0.04	-0.24 ± 0.17	-0.25 ± 0.21	–	–	1.96 ± 0.27	AGN ^{2,6}
26	10 48 35.85	+51 11 47.1	1.28	<8.60	<7.00	0.22 ± 0.07	–	–	–	–	–	AGN ²
27	10 48 38.67	+51 06 47.9	1.61	0.45 ± 0.11	<10.20	0.17 ± 0.06	–	–	–	–	2.59 ± 0.62	
28	10 48 41.34	+51 07 59.1	2.05	<13.76	<6.14	0.22 ± 0.06	–	–	–	–	–	
29	10 48 42.64	+51 06 45.5	1.73	<11.97	N	0.13 ± 0.04	0.67 ± 0.27	-0.57 ± 0.36	–	–	–	
30	10 48 44.29	+50 52 44.5	1.19	N	0.26 ± 0.07	0.45 ± 0.07	–	-0.21 ± 0.21	–	–	1.62 ± 0.42	AGN ²
31	10 48 49.01	+50 54 08.4	0.67	0.54 ± 0.10	0.39 ± 0.05	0.69 ± 0.05	-0.11 ± 0.09	-0.06 ± 0.12	–	–	1.77 ± 0.20	AGN ²
32	10 48 53.88	+51 00 34.7	1.44	0.36 ± 0.07	N	N	–	–	–	–	–	
33	10 48 59.08	+51 17 37.2	4.65	<11.79	1.29 ± 0.33	9.07 ± 1.49	–	–	–	–	7.10 ± 0.64	
34	10 49 00.32	+50 51 53.0	1.38	N	0.16 ± 0.07	N	0.02 ± 0.33	–	–	–	–	
35	10 49 00.65	+51 15 57.4	5.63	<7.61	0.66 ± 0.24	1.80 ± 0.47	–	–	–	–	2.90 ± 0.42	
36	10 49 02.34	+50 57 44.4	1.97	0.24 ± 0.07	0.13 ± 0.03	<3.56	-0.21 ± 0.27	–	–	–	1.40 ± 0.50	
37	10 49 04.45	+51 07 59.3	0.33	5.36 ± 0.14	5.19 ± 0.12	4.73 ± 0.10	-0.14 ± 0.02	-0.06 ± 0.03	-0.34 ± 0.04	-0.28 ± 0.07	1.08 ± 0.04	galaxy ⁶
38	10 49 05.16	+51 02 34.1	1.01	<5.10	0.18 ± 0.04	<3.38	-0.63 ± 0.18	–	–	–	–	
39	10 49 09.12	+51 06 57.2	0.53	0.43 ± 0.03	0.60 ± 0.03	0.62 ± 0.03	-0.32 ± 0.08	-0.22 ± 0.12	-0.06 ± 0.14	–	2.12 ± 0.17	galaxy ⁶
40	10 49 11.81	+51 08 04.8	0.24	3.23 ± 0.10	3.30 ± 0.09	3.07 ± 0.09	-0.36 ± 0.03	-0.32 ± 0.05	-0.46 ± 0.08	-0.31 ± 0.19	1.12 ± 0.05	AGN ^{1,2,3,4}
41	10 49 13.79	+50 49 24.9	2.71	<7.86	0.79 ± 0.17	0.59 ± 0.13	–	–	–	–	1.00 ± 0.34	
42	10 49 14.51	+50 55 57.4	1.20	0.29 ± 0.06	<5.16	0.32 ± 0.05	–	–	–	–	1.11 ± 0.32	

Continued on the next page

Continued from previous page

Src-NO	RA (J2000)	DEC (J2000)	r1 σ ($''$)	Flux* ** (0.2–12. keV) (10^{-13} erg s $^{-1}$ cm $^{-2}$)			Hardness ratio				Var	Classification [†]
				OBS1	OBS2	OBS3	HR1	HR2	HR3	HR4		
43	10 49 15.19	+50 56 38.0	1.47	0.29 \pm 0.04	<4.30	<4.42	-0.10 \pm 0.22	-0.14 \pm 0.25	–	–	–	
44	10 49 16.13	+51 05 37.9	1.56	0.31 \pm 0.06	0.20 \pm 0.04	0.17 \pm 0.04	-0.13 \pm 0.21	-0.59 \pm 0.29	–	–	1.57 \pm 0.48	galaxy ⁶
45	10 49 16.91	+51 03 35.8	0.74	0.34 \pm 0.03	0.32 \pm 0.03	0.32 \pm 0.02	-0.17 \pm 0.11	-0.31 \pm 0.13	–	–	1.21 \pm 0.20	Hard source
46	10 49 17.37	+51 11 00.9	1.46	0.28 \pm 0.08	0.52 \pm 0.09	0.47 \pm 0.08	–	–	–	0.58 \pm 0.13	2.13 \pm 0.47	galaxy ^{5,6}
47	10 49 18.24	+50 58 13.0	1.70	0.28 \pm 0.06	<6.20	<5.96	–	–	–	–	–	
48	10 49 20.21	+50 53 19.0	1.51	<4.24	0.34 \pm 0.07	<3.50	–	–	–	–	–	
49	10 49 20.92	+51 00 41.4	1.26	0.23 \pm 0.02	0.15 \pm 0.03	0.17 \pm 0.02	-0.40 \pm 0.14	-0.25 \pm 0.23	–	–	1.29 \pm 0.38	AGN ^{1,4}
50	10 49 20.77	+51 06 10.0	1.19	0.72 \pm 0.05	0.78 \pm 0.04	0.63 \pm 0.05	-0.24 \pm 0.08	-0.18 \pm 0.11	-0.46 \pm 0.13	–	1.69 \pm 0.14	Hard source
51	10 49 21.93	+50 57 12.0	1.17	0.28 \pm 0.03	0.30 \pm 0.03	0.30 \pm 0.03	–	0.49 \pm 0.16	-0.39 \pm 0.15	–	1.24 \pm 0.21	AGN ²
52	10 49 22.24	+51 15 10.4	1.32	0.65 \pm 0.13	0.77 \pm 0.12	0.42 \pm 0.07	-0.02 \pm 0.22	-0.01 \pm 0.20	–	–	1.88 \pm 0.31	AGN ²
53	10 49 23.67	+50 57 43.7	1.29	0.24 \pm 0.05	0.16 \pm 0.02	0.20 \pm 0.02	-0.19 \pm 0.19	0.01 \pm 0.22	-0.07 \pm 0.23	–	1.40 \pm 0.32	AGN ²
54	10 49 25.23	+50 55 57.5	1.95	0.19 \pm 0.06	<8.29	<7.19	–	–	–	–	–	
55	10 49 26.50	+50 51 15.0	1.01	0.44 \pm 0.06	0.54 \pm 0.06	0.61 \pm 0.05	–	0.32 \pm 0.15	-0.01 \pm 0.14	–	1.16 \pm 0.20	Hard source
56	10 49 27.41	+50 55 14.3	1.48	0.25 \pm 0.07	0.32 \pm 0.07	0.31 \pm 0.06	-0.34 \pm 0.17	–	–	–	1.11 \pm 0.48	galaxy ⁶
57	10 49 27.67	+51 03 43.1	1.67	0.27 \pm 0.06	0.16 \pm 0.02	0.16 \pm 0.02	0.04 \pm 0.20	-0.13 \pm 0.19	–	–	1.41 \pm 0.42	Symbiotic star
58	10 49 27.90	+51 05 49.9	1.29	0.29 \pm 0.03	0.18 \pm 0.02	0.19 \pm 0.02	-0.35 \pm 0.17	-0.17 \pm 0.24	–	–	1.37 \pm 0.24	
59	10 49 31.43	+51 03 03.1	0.78	0.35 \pm 0.03	0.32 \pm 0.03	0.33 \pm 0.03	-0.21 \pm 0.09	-0.14 \pm 0.11	-0.51 \pm 0.15	–	1.18 \pm 0.18	AGN ^{1,3,4}
60	10 49 32.18	+51 13 17.3	2.19	0.41 \pm 0.07	0.33 \pm 0.06	0.25 \pm 0.05	–	–	–	–	1.53 \pm 0.29	AGN ^{2,6}
61	10 49 33.55	+51 04 20.1	0.78	0.28 \pm 0.04	0.32 \pm 0.03	0.35 \pm 0.04	-0.19 \pm 0.09	-0.03 \pm 0.11	-0.51 \pm 0.13	–	1.06 \pm 0.24	Hard source
62	10 49 34.16	+51 00 41.5	1.60	0.44 \pm 0.07	0.21 \pm 0.02	0.18 \pm 0.02	-0.22 \pm 0.17	-0.48 \pm 0.33	-0.35 \pm 0.25	–	2.51 \pm 0.30	Hard source
63	10 49 35.72	+50 55 19.8	2.09	<8.60	<7.06	0.25 \pm 0.06	–	–	–	–	–	
64	10 49 37.81	+51 11 23.8	1.98	0.42 \pm 0.06	0.37 \pm 0.05	<3.56	–	–	–	–	1.41 \pm 0.31	AGN ^{1,3,4}
65	10 49 40.31	+50 58 40.6	0.95	0.33 \pm 0.04	0.34 \pm 0.03	0.26 \pm 0.02	-0.37 \pm 0.12	–	–	–	2.23 \pm 0.19	Foreground star
66	10 49 42.29	+51 04 27.5	1.37	0.21 \pm 0.05	0.14 \pm 0.04	0.28 \pm 0.04	-0.45 \pm 0.15	–	–	–	1.93 \pm 0.44	
67	10 49 43.05	+51 01 44.8	0.94	0.28 \pm 0.03	0.23 \pm 0.03	0.27 \pm 0.02	–	–	-0.34 \pm 0.12	-0.07 \pm 0.20	1.57 \pm 0.25	Hard source
68	10 49 44.60	+51 09 00.3	1.55	N	0.23 \pm 0.04	<3.44	–	–	–	–	–	galaxy ⁶
69	10 49 46.66	+50 58 24.5	0.72	0.46 \pm 0.07	0.51 \pm 0.05	0.56 \pm 0.04	–	0.46 \pm 0.09	-0.30 \pm 0.09	–	2.06 \pm 0.23	AGN ²
70	10 49 46.89	+51 05 14.8	0.40	1.42 \pm 0.07	1.34 \pm 0.05	1.21 \pm 0.05	-0.22 \pm 0.05	-0.15 \pm 0.07	-0.20 \pm 0.08	-0.37 \pm 0.13	1.97 \pm 0.08	AGN ^{1,2,3,4}
71	10 49 47.06	+50 58 59.1	1.39	0.43 \pm 0.05	0.48 \pm 0.05	0.46 \pm 0.04	-0.11 \pm 0.12	-0.03 \pm 0.15	-0.40 \pm 0.18	–	1.12 \pm 0.23	AGN ^{1,2,3,4}
72	10 49 47.73	+51 02 19.8	1.32	0.18 \pm 0.05	0.18 \pm 0.03	0.18 \pm 0.02	–	0.27 \pm 0.19	-0.20 \pm 0.19	-0.05 \pm 0.25	1.59 \pm 0.38	galaxy ⁶
73	10 49 48.94	+51 00 01.2	0.90	<6.82	0.21 \pm 0.04	0.23 \pm 0.02	-0.11 \pm 0.12	0.01 \pm 0.15	-0.35 \pm 0.17	–	1.08 \pm 0.33	AGN ^{1,2,3,4}
74	10 49 50.40	+51 09 06.5	1.83	<8.41	0.21 \pm 0.05	<5.10	–	–	–	–	–	galaxy ⁶
75	10 49 50.53	+51 10 00.8	1.26	0.24 \pm 0.07	N	0.21 \pm 0.06	-0.19 \pm 0.27	–	–	–	1.89 \pm 0.62	
76	10 49 51.56	+51 15 32.6	1.47	0.93 \pm 0.19	1.03 \pm 0.17	0.31 \pm 0.08	–	0.27 \pm 0.24	-0.19 \pm 0.25	–	2.84 \pm 0.44	Hard source
77	10 49 51.36	+50 51 50.4	1.09	N	0.52 \pm 0.08	0.48 \pm 0.05	-0.08 \pm 0.13	-0.12 \pm 0.17	–	–	1.08 \pm 0.26	galaxy ^{5,6}
78	10 49 52.10	+50 50 16.5	1.84	<6.27	<4.55	0.19 \pm 0.06	–	–	–	–	–	
79	10 49 54.59	+51 05 33.5	1.94	0.55 \pm 0.06	0.56 \pm 0.04	0.35 \pm 0.04	-0.31 \pm 0.07	-0.27 \pm 0.11	-0.28 \pm 0.16	–	1.56 \pm 0.17	galaxy ^{5,6}
80	10 49 55.99	+51 04 49.3	1.02	0.24 \pm 0.04	0.18 \pm 0.04	0.35 \pm 0.03	-0.20 \pm 0.11	-0.03 \pm 0.15	-0.57 \pm 0.18	-0.24 \pm 0.27	1.81 \pm 0.33	galaxy ⁶
81	10 49 59.73	+51 01 21.7	1.80	N	0.17 \pm 0.05	0.17 \pm 0.05	–	0.27 \pm 0.26	-0.65 \pm 0.32	–	1.19 \pm 0.56	Hard source
82	10 50 00.33	+50 56 03.0	0.96	0.72 \pm 0.08	0.69 \pm 0.06	0.39 \pm 0.04	-0.23 \pm 0.12	-0.32 \pm 0.16	-0.05 \pm 0.22	–	1.86 \pm 0.18	AGN ^{1,2,3,4}
83	10 50 06.53	+51 05 22.9	1.25	0.75 \pm 0.07	0.67 \pm 0.06	0.42 \pm 0.06	-0.25 \pm 0.10	-0.14 \pm 0.13	-0.35 \pm 0.16	–	1.73 \pm 0.24	AGN ^{2,6}
84	10 50 06.93	+51 08 11.5	2.46	0.35 \pm 0.09	0.39 \pm 0.07	0.26 \pm 0.07	-0.35 \pm 0.15	-0.67 \pm 0.27	–	–	1.55 \pm 0.44	
85	10 50 08.82	+51 02 53.0	0.64	0.90 \pm 0.06	1.33 \pm 0.08	0.68 \pm 0.04	-0.12 \pm 0.10	-0.05 \pm 0.10	-0.35 \pm 0.11	–	1.90 \pm 0.13	AGN ^{2,6,4}
86	10 50 09.15	+51 12 10.6	0.84	0.80 \pm 0.14	0.20 \pm 0.07	0.62 \pm 0.10	–	–	0.17 \pm 0.18	-0.04 \pm 0.22	2.39 \pm 0.48	galaxy ^{5,6}
87	10 50 09.77	+51 02 37.4	0.95	0.45 \pm 0.06	0.31 \pm 0.05	0.31 \pm 0.04	-0.15 \pm 0.27	-0.14 \pm 0.23	–	–	3.94 \pm 0.23	AGN ²

Continued on the next page

Src-NO	RA (J2000)	DEC (J2000)	r1 σ (")	Flux* ** (0.2–12. keV) (10^{-13} erg s $^{-1}$ cm $^{-2}$)			Hardness ratio				Var	Classification [†]
				OBS1	OBS2	OBS3	HR1	HR2	HR3	HR4		
88	10 50 10.27	+50 56 42.9	1.37	0.26 \pm 0.06	0.46 \pm 0.09	0.25 \pm 0.04	–	–	-0.24 \pm 0.16	–	1.87 \pm 0.33	galaxy ^{5,6}
89	10 50 11.67	+50 59 43.5	0.94	0.46 \pm 0.05	0.42 \pm 0.04	0.35 \pm 0.04	-0.16 \pm 0.13	-0.02 \pm 0.15	-0.32 \pm 0.18	–	1.13 \pm 0.21	galaxy ⁶
90	10 50 12.05	+51 06 16.0	0.81	1.01 \pm 0.09	0.82 \pm 0.06	0.80 \pm 0.06	-0.25 \pm 0.09	-0.20 \pm 0.12	–	–	1.37 \pm 0.17	AGN ¹
91	10 50 13.46	+51 10 55.4	1.49	0.46 \pm 0.10	0.86 \pm 0.08	0.43 \pm 0.06	–	–	–	–	2.14 \pm 0.24	galaxy ^{5,6}
92	10 50 13.57	+51 00 10.5	6.70	1.29 \pm 0.24	0.24 \pm 0.06	0.76 \pm 0.15	–	–	–	–	5.51 \pm 0.46	
93	10 50 22.62	+51 06 00.5	1.39	0.29 \pm 0.07	0.41 \pm 0.09	0.27 \pm 0.05	–	0.78 \pm 0.19	-0.12 \pm 0.18	0.14 \pm 0.28	1.77 \pm 0.41	Hard source
94	10 50 23.25	+50 54 42.0	1.12	<14.31	0.43 \pm 0.09	<6.88	-0.13 \pm 0.24	–	–	–	–	
95	10 50 25.57	+51 02 50.0	1.99	<9.76	0.27 \pm 0.07	0.27 \pm 0.07	-0.16 \pm 0.27	0.03 \pm 0.31	–	–	1.03 \pm 0.52	galaxy ⁶
96	10 50 27.00	+51 06 32.8	1.55	0.25 \pm 0.08	N	0.24 \pm 0.04	–	0.23 \pm 0.19	–	–	1.27 \pm 0.38	galaxy ^{5,6}
97	10 50 42.20	+50 58 07.9	1.51	0.53 \pm 0.13	0.51 \pm 0.08	0.48 \pm 0.06	–	0.44 \pm 0.18	-0.43 \pm 0.18	–	3.71 \pm 0.46	Hard source

[†]: Sources, which are classified in the optical/infrared studies as AGNs or background galaxies. References of the class of object in the available catalogues are (1): The Million Quasars catalogue (Flesch 2019), (2): The WISE AGN candidates catalogs (Assef et al. 2018), (3): Quasars selection from SDSS and WISE surveys (Richards et al. 2015), (4): known QSOs for the Gaia mission (Liao et al. 2019), (5): Star/Galaxy Separation (Vasconcellos et al. 2011), and (6): SDSS11/12 spectroscopic data (Alam et al. 2015).

The details of the publications are given Sect. 4.3. For all these sources the classification was consistent with the classification based on our criteria for background sources.

*: '<' means 3 σ upper limits are reported in case of non-detection of the source in the 0.2–12.0 keV band in EPIC-pn and EPIC-MOS cameras.

**: 'N' means that source is located on the gap, damaged pixel, or outside the EPIC field of view.

Table A2. Optical magnitudes of counterparts of X-ray sources of Wil 1 in different energy filters of the SDSS12 survey.

Src-No	<i>u</i> mag	<i>g</i> mag	<i>r</i> mag	<i>i</i> mag	<i>z</i> mag
2	21.45 ± 0.16	21.09 ± 0.04	20.76 ± 0.05	20.24 ± 0.05	20.18 ± 0.17
3	21.58 ± 0.11	20.75 ± 0.02	20.51 ± 0.03	20.44 ± 0.04	20.25 ± 0.11
4	20.58 ± 0.06	20.24 ± 0.02	19.67 ± 0.02	19.22 ± 0.02	18.77 ± 0.04
6	22.17 ± 0.21	21.64 ± 0.05	21.45 ± 0.05	21.34 ± 0.08	20.44 ± 0.13
7	23.71 ± 0.64	22.80 ± 0.14	22.38 ± 0.15	22.32 ± 0.23	21.59 ± 0.37
8	22.11 ± 0.20	21.37 ± 0.04	20.82 ± 0.03	20.62 ± 0.04	20.61 ± 0.15
9	22.26 ± 0.24	21.68 ± 0.06	21.28 ± 0.07	20.50 ± 0.05	20.29 ± 0.15
14	23.83 ± 0.61	24.05 ± 0.37	23.74 ± 0.44	22.18 ± 0.18	21.57 ± 0.34
17	24.68 ± 1.15	23.89 ± 0.41	22.34 ± 0.18	22.27 ± 0.29	23.03 ± 0.76
18	20.54 ± 0.05	20.52 ± 0.02	20.74 ± 0.03	20.55 ± 0.04	20.48 ± 0.14
19	25.61 ± 0.66	21.56 ± 0.04	20.86 ± 0.03	20.81 ± 0.05	20.53 ± 0.14
20	21.06 ± 0.07	21.00 ± 0.03	21.21 ± 0.05	20.99 ± 0.06	20.81 ± 0.17
23	20.07 ± 0.04	19.85 ± 0.01	19.73 ± 0.01	19.55 ± 0.02	19.55 ± 0.06
25	22.67 ± 0.29	22.21 ± 0.09	22.10 ± 0.12	21.38 ± 0.11	20.86 ± 0.22
26	25.36 ± 0.94	23.62 ± 0.29	22.58 ± 0.18	22.25 ± 0.22	22.46 ± 0.70
28	24.10 ± 1.80	22.14 ± 0.15	21.69 ± 0.15	20.78 ± 0.11	20.55 ± 0.34
31	23.91 ± 0.61	23.62 ± 0.25	23.99 ± 0.45	22.96 ± 0.34	22.80 ± 0.55
37	25.78 ± 0.58	22.63 ± 0.11	21.80 ± 0.08	20.99 ± 0.06	20.33 ± 0.12
39	22.92 ± 0.30	22.20 ± 0.08	22.17 ± 0.11	21.49 ± 0.10	21.69 ± 0.35
40	18.93 ± 0.02	18.74 ± 0.01	18.78 ± 0.01	18.87 ± 0.01	18.75 ± 0.03
44	23.58 ± 0.74	23.10 ± 0.26	22.43 ± 0.21	23.71 ± 0.97	22.20 ± 0.78
46	18.73 ± 0.03	17.24 ± 0.01	16.56 ± 0.01	16.13 ± 0.01	15.91 ± 0.01
49	22.32 ± 0.18	21.07 ± 0.03	21.04 ± 0.04	20.85 ± 0.06	20.82 ± 0.17
50	22.56 ± 0.23	22.40 ± 0.09	21.73 ± 0.07	21.66 ± 0.12	21.41 ± 0.28
52	22.04 ± 0.21	22.53 ± 0.12	21.78 ± 0.09	21.8 ± 0.16	21.29 ± 0.35
56	23.06 ± 0.52	23.15 ± 0.23	21.94 ± 0.12	21.46 ± 0.13	20.63 ± 0.21
57	21.88 ± 0.13	20.75 ± 0.02	20.34 ± 0.02	20.22 ± 0.03	19.95 ± 0.08
59	21.68 ± 0.11	21.50 ± 0.04	21.35 ± 0.05	21.25 ± 0.09	20.83 ± 0.19
60	25.58 ± 1.10	23.46 ± 0.38	21.78 ± 0.13	21.07 ± 0.12	20.07 ± 0.17
64	20.32 ± 0.05	20.17 ± 0.01	20.05 ± 0.02	20.14 ± 0.03	20.10 ± 0.10
65	21.49 ± 0.09	19.02 ± 0.00	17.60 ± 0.01	16.62 ± 0.01	16.10 ± 0.01
68	23.76 ± 0.78	24.16 ± 0.56	23.71 ± 0.58	21.86 ± 0.20	21.49 ± 0.47
70	20.79 ± 0.05	20.56 ± 0.02	20.51 ± 0.02	20.63 ± 0.05	20.38 ± 0.12
71	20.44 ± 0.04	20.19 ± 0.01	20.12 ± 0.02	19.91 ± 0.02	19.94 ± 0.08
72	22.99 ± 0.38	23.93 ± 0.41	23.53 ± 0.43	21.82 ± 0.17	21.02 ± 0.26
73	19.70 ± 0.02	19.59 ± 0.01	19.49 ± 0.01	19.35 ± 0.01	19.10 ± 0.04
74	24.92 ± 0.84	24.01 ± 0.43	22.21 ± 0.14	21.48 ± 0.12	21.34 ± 0.34
77	20.81 ± 0.09	20.21 ± 0.02	19.29 ± 0.01	18.86 ± 0.01	18.50 ± 0.04
78	24.84 ± 0.80	23.68 ± 0.27	22.02 ± 0.09	21.28 ± 0.08	21.27 ± 0.27
79	21.31 ± 0.09	20.86 ± 0.03	20.84 ± 0.04	20.63 ± 0.06	20.54 ± 0.17
80	22.98 ± 0.42	22.91 ± 0.20	23.27 ± 0.40	22.22 ± 0.27	21.56 ± 0.47
82	20.86 ± 0.07	20.61 ± 0.02	20.41 ± 0.02	20.37 ± 0.03	20.40 ± 0.15
83	22.12 ± 0.17	22.02 ± 0.07	21.39 ± 0.06	21.27 ± 0.09	21.22 ± 0.28
84	23.94 ± 0.69	22.75 ± 0.14	22.69 ± 0.21	22.54 ± 0.29	21.63 ± 0.40
85	23.93 ± 0.65	22.61 ± 0.12	21.11 ± 0.05	20.42 ± 0.04	20.11 ± 0.10
86	23.26 ± 0.61	20.84 ± 0.03	19.87 ± 0.02	19.45 ± 0.02	19.19 ± 0.05
88	20.02 ± 0.06	18.97 ± 0.01	18.22 ± 0.01	17.81 ± 0.01	17.54 ± 0.02
89	21.56 ± 0.11	21.60 ± 0.05	21.53 ± 0.07	21.30 ± 0.09	21.38 ± 0.33
90	22.12 ± 0.17	21.96 ± 0.07	21.73 ± 0.08	21.39 ± 0.10	21.30 ± 0.29
91	21.45 ± 0.09	21.04 ± 0.03	20.59 ± 0.03	20.34 ± 0.03	19.82 ± 0.08
92	23.33 ± 0.41	21.27 ± 0.03	20.06 ± 0.02	19.58 ± 0.02	19.44 ± 0.05
95	24.75 ± 1.55	22.72 ± 0.26	21.53 ± 0.14	21.13 ± 0.16	20.55 ± 0.31
96	21.79 ± 0.17	21.31 ± 0.05	19.82 ± 0.02	19.28 ± 0.02	18.95 ± 0.06

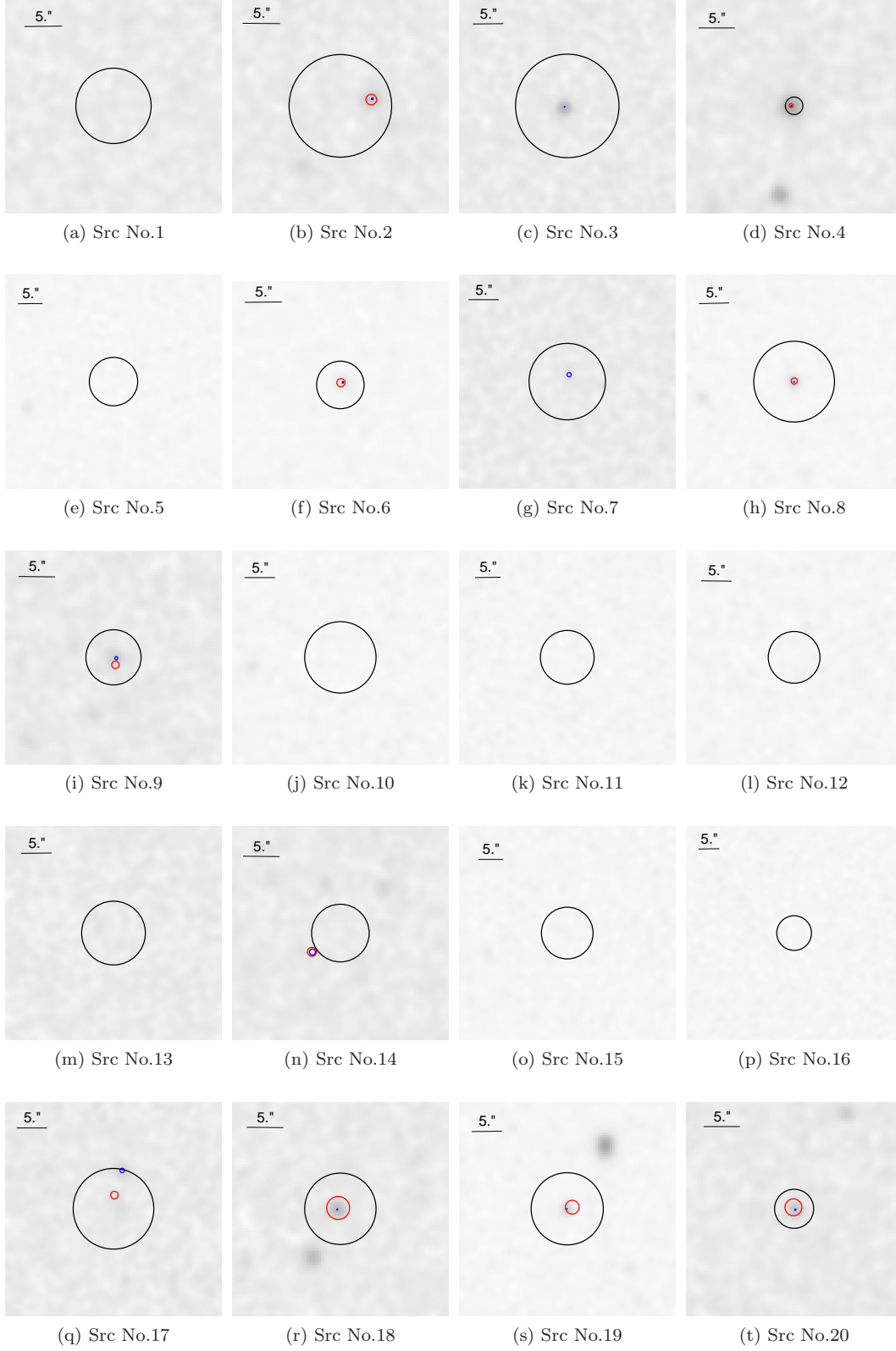
Table A3. Infrared magnitudes of counterparts of X-ray sources of Wil 1 in different energy filters 2MASS and WISE surveys.

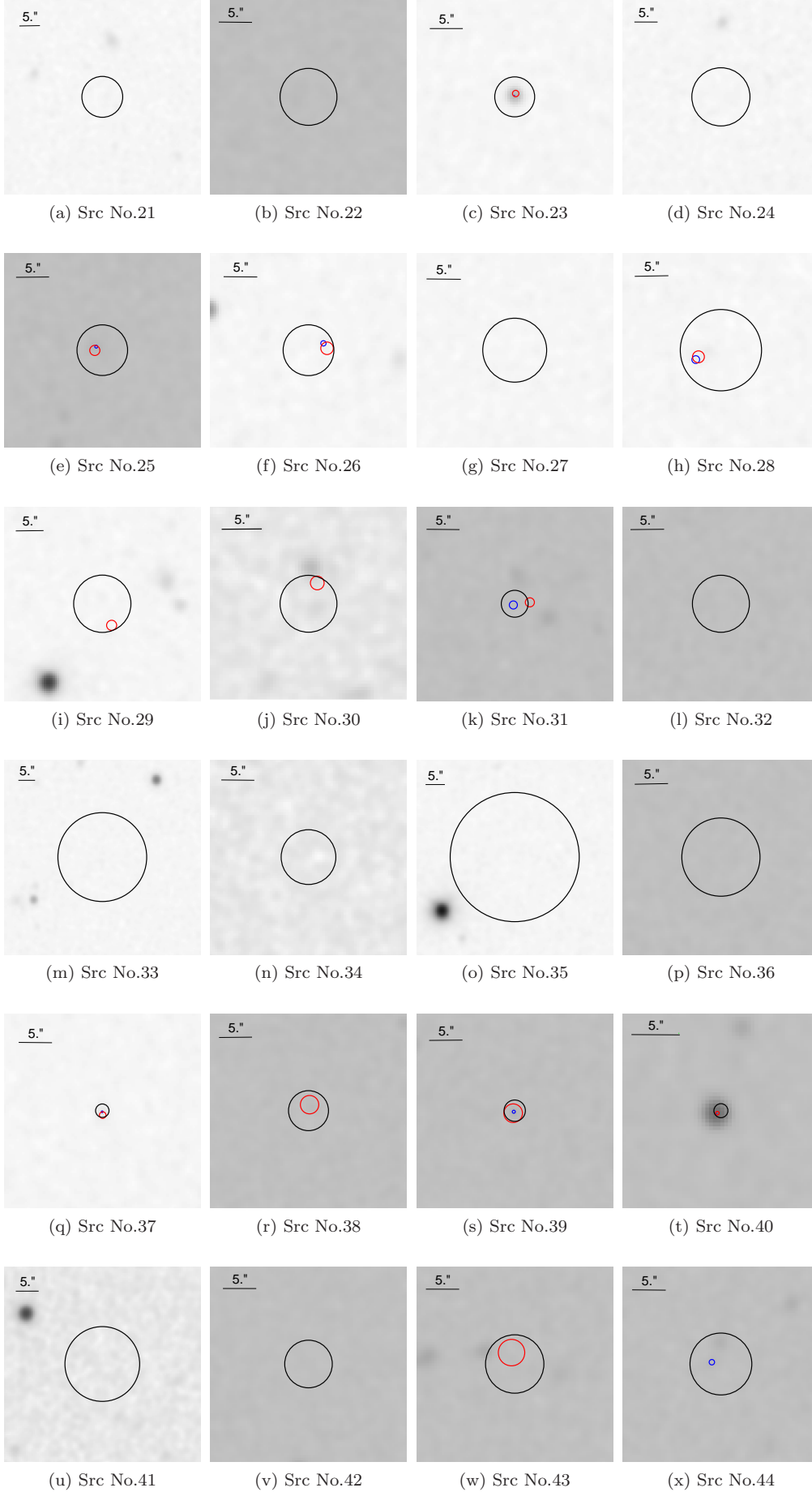
Src-No	<i>J</i> mag	<i>H</i> mag	<i>K</i> mag	W1 mag	W2 mag	W3 mag	W4 mag
2				16.77 ± 0.08	15.98 ± 0.15	<12.69*	<9.06*
4				15.34 ± 0.03	14.59 ± 0.05	12.29 ± 0.33	<8.53*
6				16.33 ± 0.06	15.94 ± 0.13	<12.40*	<8.34*
8				16.40 ± 0.06	15.36 ± 0.08	<12.29*	<8.79*
9				16.23 ± 0.06	15.68 ± 0.12	<12.18*	<8.83*
14				16.65 ± 0.07	15.89 ± 0.12	<12.83*	<9.32*
17				16.54 ± 0.07	15.82 ± 0.12	<12.63*	<9.13*
18				17.89 ± 0.21	16.34 ± 0.20	<12.17*	<9.09*
19				17.46 ± 0.14	16.26 ± 0.17	12.41 ± 0.43	<8.91*
20				17.38 ± 0.14	16.26 ± 0.17	<12.55*	<8.64*
23				16.43 ± 0.06	15.03 ± 0.07	12.52 ± 0.44	8.78 ± 0.37
25				16.83 ± 0.08	16.02 ± 0.15	<12.08*	<8.90*
26				17.10 ± 0.10	16.30 ± 0.18	<12.40*	<8.80*
28				16.88 ± 0.09	16.84 ± 0.31	<12.21*	<9.09*
29				16.91 ± 0.09	<16.78*	<12.44*	<9.08*
30				17.08 ± 0.10	16.09 ± 0.15	12.64 ± 0.45	<8.87*
31				16.76 ± 0.08	15.92 ± 0.13	12.51 ± 0.44	<8.78*
37				16.23 ± 0.05	16.36 ± 0.18	<12.87*	<9.13*
38				17.54 ± 0.15	16.84 ± 0.29	<12.36*	<8.86*
39				17.46 ± 0.15	16.79 ± 0.30	<12.43*	<8.77*
40				14.87 ± 0.03	13.81 ± 0.03	11.33 ± 0.14	8.59 ± 0.24
43				17.86 ± 0.20	<16.78*	<12.67*	<8.86*
45				16.63 ± 0.07	15.64 ± 0.10	12.47 ± 0.42	<8.86 *
46	15.76 ± 0.11	15.28 ± 0.13	14.62 ± 0.10	13.79 ± 0.04	13.38 ± 0.05	9.56 ± 0.06	7.08 ± 0.13
50				16.14 ± 0.06	15.55 ± 0.13	12.59 ± 0.50	9.29 ± 0.52
51				17.42 ± 0.14	16.43 ± 0.21	<12.31*	<9.18*
52				16.90 ± 0.08	16.14 ± 0.16	<12.79*	<9.12*
53				16.88 ± 0.09	16.06 ± 0.15	<12.69*	<9.12*
56				16.92 ± 0.10	16.55 ± 0.24	<12.71*	<8.76*
58				17.45 ± 0.15	16.64 ± 0.26	<12.45*	<8.46*
59				17.77 ± 0.19	17.19 ± 0.39	<12.20*	<8.71*
60				15.66 ± 0.04	14.60 ± 0.04	11.51 ± 0.17	9.00 ± 0.46
65	14.81 ± 0.04	14.23 ± 0.04	13.95 ± 0.04	13.83 ± 0.03	13.69 ± 0.03	12.54 ± 0.53	<9.07*
67				17.13 ± 0.11	16.54 ± 0.24	<12.14*	<8.76*
69				17.72 ± 0.18	16.16 ± 0.17	12.06 ± 0.33	<8.54*
71				15.57 ± 0.04	14.65 ± 0.05	12.46 ± 0.47	<8.39*
72				16.60 ± 0.07	16.12 ± 0.16	<12.74*	<9.06*
73				16.03 ± 0.05	14.60 ± 0.05	10.99 ± 0.12	<8.64*
77				15.45 ± 0.03	15.12 ± 0.07	12.46 ± 0.42	<8.46*
79				16.70 ± 0.08	16.33 ± 0.19	<12.29*	<8.96*
82				16.31 ± 0.06	15.23 ± 0.07	12.52 ± 0.46	<8.59*
83				16.58 ± 0.07	15.56 ± 0.10	<12.41*	<9.07*
85				15.21 ± 0.03	13.96 ± 0.03	11.56 ± 0.21	<8.42*
86				15.69 ± 0.04	15.07 ± 0.06	12.71 ± 0.46	<9.22*
87				16.96 ± 0.09	15.86 ± 0.12	<12.63*	<8.52*
88	16.72 ± 0.14	<15.67*	15.40 ± 0.18	14.90 ± 0.03	14.63 ± 0.06	11.05 ± 0.12	<9.07*
89				15.80 ± 0.04	15.60 ± 0.10	12.31 ± 0.37	<8.78*
90				16.38 ± 0.06	16.08 ± 0.15	12.64 ± 0.42	<8.61*
91				16.38 ± 0.05	15.95 ± 0.12	<12.47*	<8.80*
95				17.48 ± 0.14	16.62 ± 0.24	<12.79*	<9.10*
96				15.50 ± 0.04	15.20 ± 0.07	12.28 ± 0.34	<8.51*
97				15.66 ± 0.04	15.01 ± 0.07	<12.02*	<8.55*

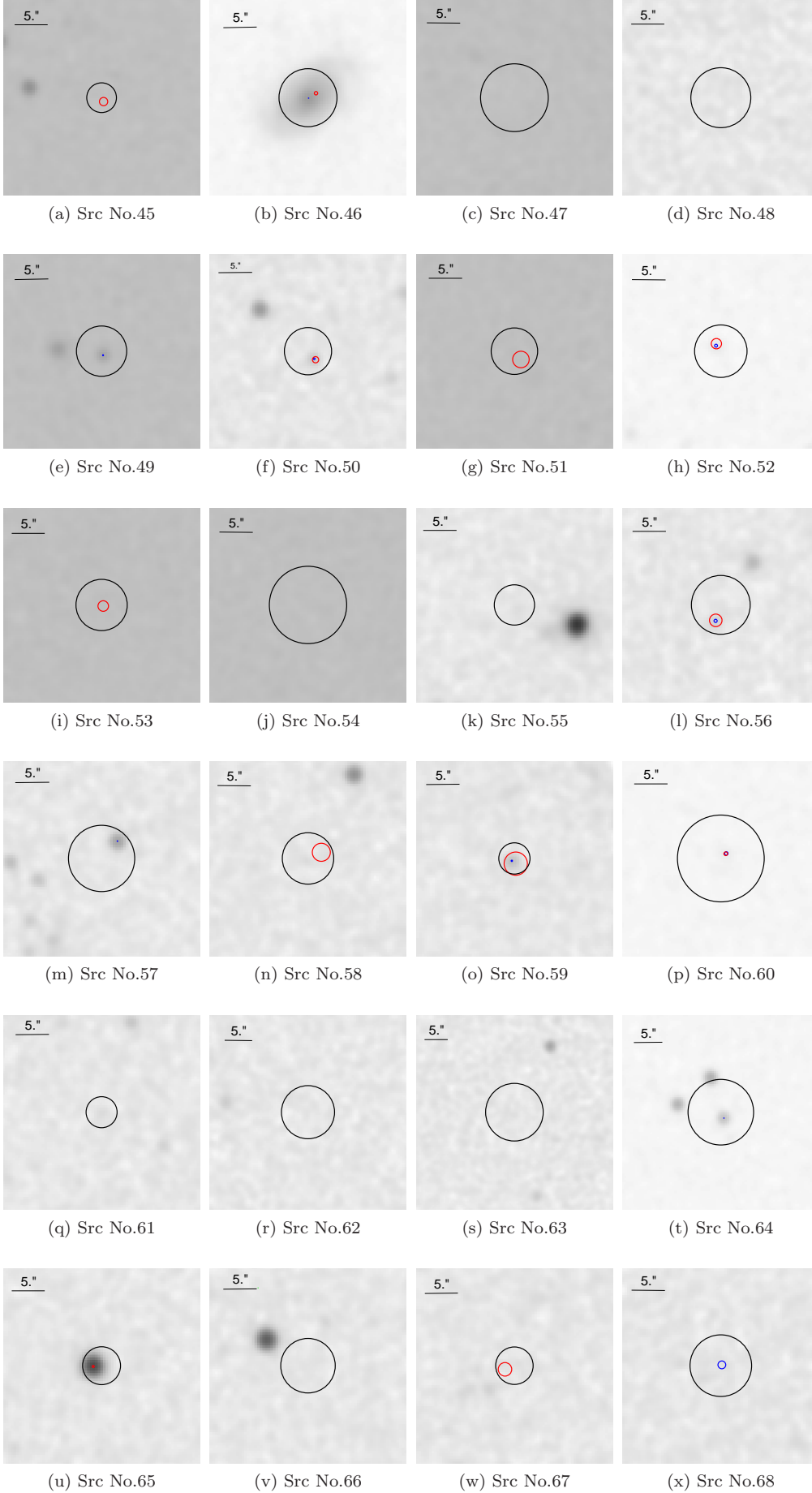
*: Upper limit reported in the WISE catalogue.

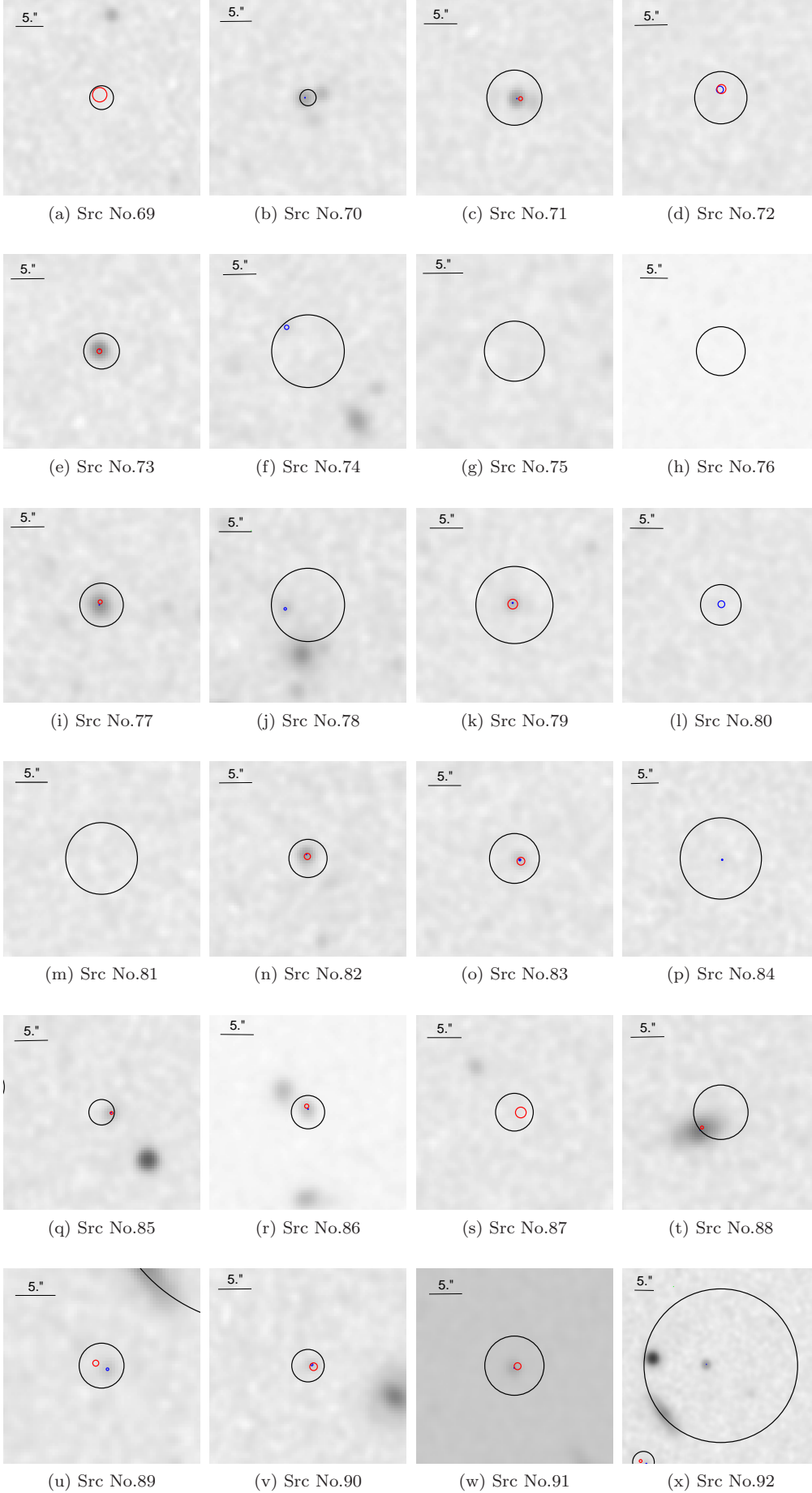
APPENDIX B: IMAGE OF OPTICAL SDSS9 COUNTERPARTS

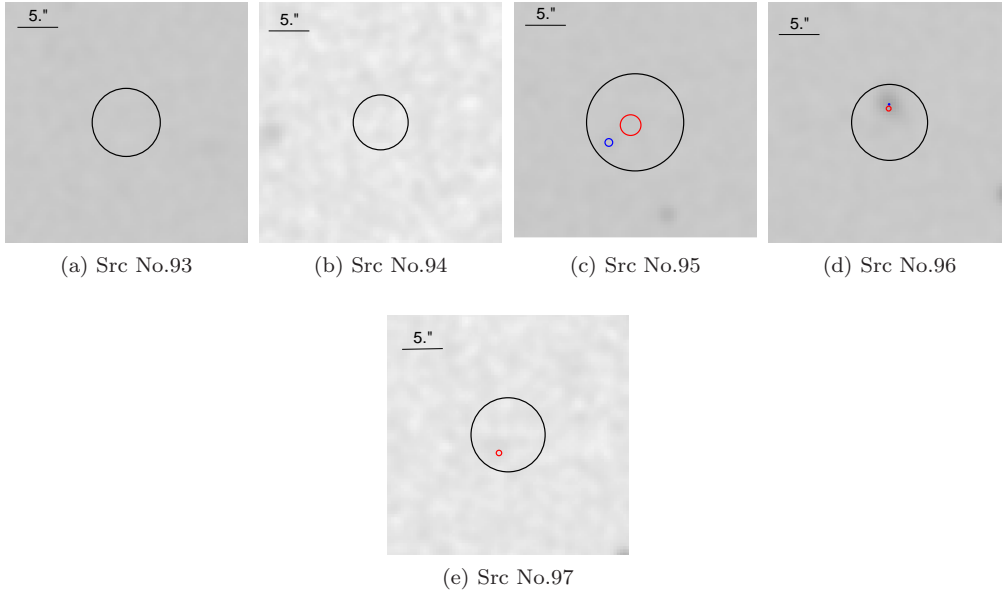
The optical image of the counterpart of the X-ray sources from the SDSS9 survey. The images are the r band of SDSS survey. Images shows 3σ circle error of X-ray sources (black), optical counterparts (blue) and infrared counterpart (red).











This paper has been typeset from a \LaTeX file prepared by the author.